Volume 5
Number 1
7 January 2024
Pages 1–380

Materials Advances

rsc.li/materials-advances

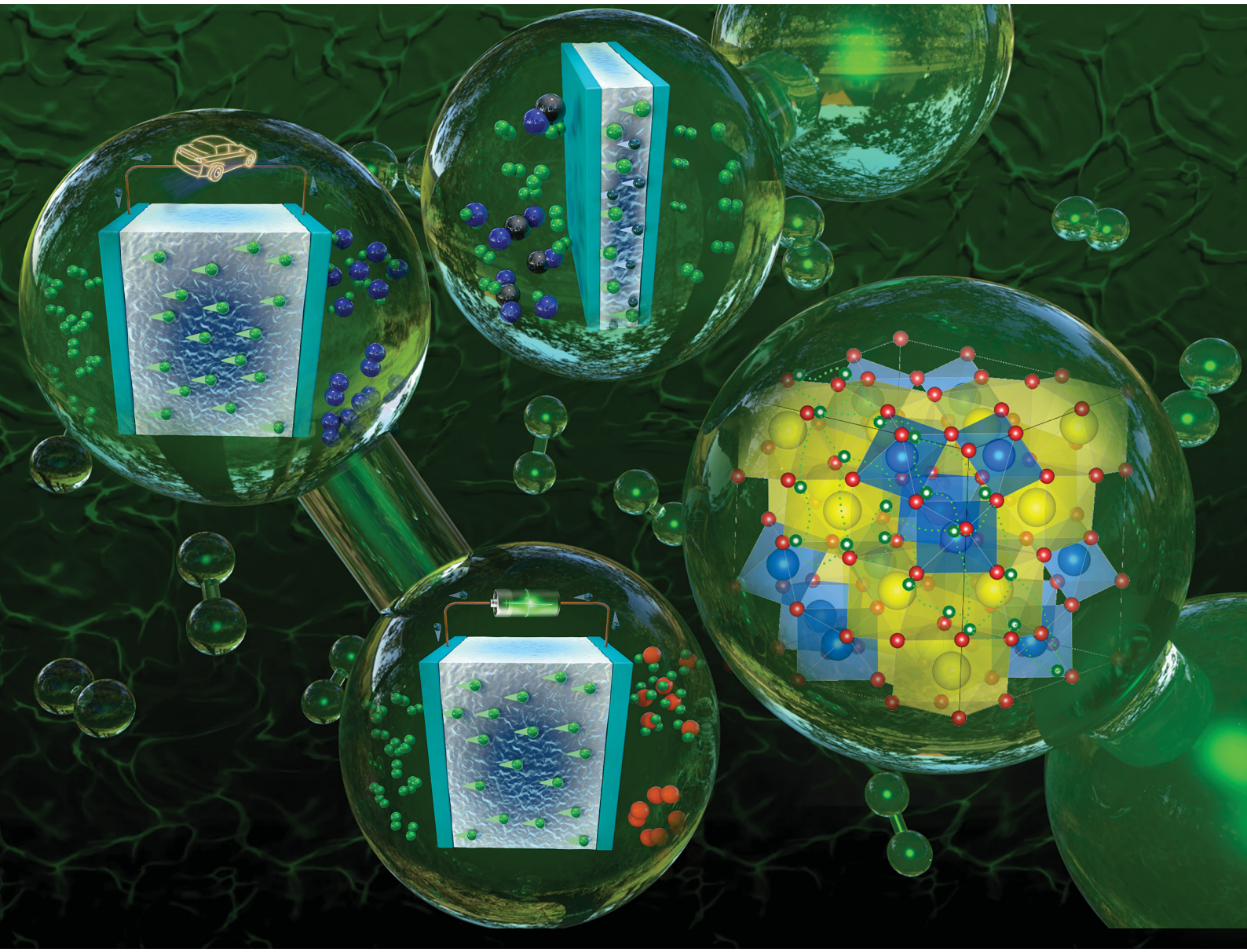

ISSN 2633-5409

ROYAL SOCIETY OF CHEMISTRY

REVIEW ARTICLE
Donglin Han *et al.*
Fluorite-based proton conducting oxides: structures, materials and applications

Materials Advances

ROYAL SOCIETY OF CHEMISTRY

REVIEW

View Article Online
View Journal | View Issue

Check for updates

Cite this: *Mater. Adv.*, 2024, 5, 12

Fluorite-based proton conducting oxides: structures, materials and applications

Pan Xiang,†[a] Sara Adeeba Ismail,†[a] Shihang Guo,[a] Lulu Jiang[a] and Donglin Han *[abc]

Received 5th July 2023,
Accepted 7th September 2023

DOI: 10.1039/d3ma00367a

rsc.li/materials-advances

Proton conducting oxides have promising potential for application in solid-state electrochemical devices and have seen significant progress in recent years. At present, perovskite-type proton conductors (*e.g.*, Y-doped Ba(Zr, Ce)O_3) attract much attention. However, in fact, those with a fluorite-based structure constitute another interesting category, including doped zirconia and ceria with a fluorite structure, and lanthanide zirconates, stannates, and titanates with a pyrochlore structure. In this work, we focus on the volume transport of protons in fluorite and pyrochlore oxides, summarize the progress on the development of materials and their applications, and discuss the present problems and challenges ahead.

1. Introduction

Proton conducting oxide ceramics are attracting increasing attention due to their promising applications as electrolyte materials in fuel cells,[1] electrolysis cells,[2] hydrogen sensors,[3] hydrogen pumps,[4] hydrogen permeation membranes,[5] and membrane reactors.[6] The most successful proton conducting oxide ceramics have an ABO_3 perovskite structure, including acceptor-doped $BaZrO_3$, $BaCeO_3$ and Ba(Zr, Ce)O_3 solid solutions,[7–9] which contain oxygen vacancies ($V_O^{\bullet\bullet}$) favoring hydration reactions to introduce protons:

$$H_2O + O_O^{\times} + V_O^{\bullet\bullet} = 2OH_O^{\bullet} \quad (1)$$

Here, $O_O^{\times}$ is the Kröger–Vink notation for oxide ions, and $OH_O^{\bullet}$ represents protons, which are associated with oxide ions. Protons rotate around and hop between lattice oxide ions to facilitate proton conduction, which is commonly known as the Grotthuss mechanism.

Besides, some other oxides with crystal structures of fluorite and pyrochlore, which can be regarded as an ordered fluorite structure, are also known to demonstrate proton conduction. As shown in Fig. 1(a), in the fluorite structure taking an AO_2 formula, cations occupy the corners and face centers (Wyckoff 4a site) of the unit cell, and oxide ions occupy the center of the tetrahedrons (8c site) composing four cations. All the cations and oxide ions (also oxygen vacancies) are randomly

[a] *College of Energy, Soochow University, No 1 Shizi Street, Gusu District, Suzhou 215006, China. E-mail: dlhan@suda.edu.cn*
[b] *Provincial Key Laboratory for Advanced Carbon Materials and Wearable Energy Technologies, Soochow University, No 1 Shizi Street, Gusu District, Suzhou 215006, China*
[c] *Light Industry Institute of Electrochemical Power Sources, Shahu Science & Technology Innovation Park, Suzhou 215638, China*
† These authors contributed equally.

Pan Xiang

Pan Xiang is currently an undergraduate student at the College of Energy, Soochow University under the supervision of Prof. Donglin Han. His research interest is proton conducting oxides.

Sara Adeeba Ismail

Sara Adeeba Ismail is currently pursuing her PhD degree at Soochow University. She received her Master's Degree in new energy science and engineering from the College of Energy at Soochow University China (2019–2022). Her study focuses on the synthesis and utilization of electrolyte material for ceramic-based fuel cells.

Open Access Article. Published on 08 September 2023. Downloaded on 6/11/2026 10:35:40 PM.
This article is licensed under a Creative Commons Attribution 3.0 Unported Licence.

© 2024 The Author(s). Published by the Royal Society of Chemistry

Open Access Article. Published on 08 September 2023. Downloaded on 6/11/2026 10:35:40 PM.
This article is licensed under a Creative Commons Attribution 3.0 Unported Licence.

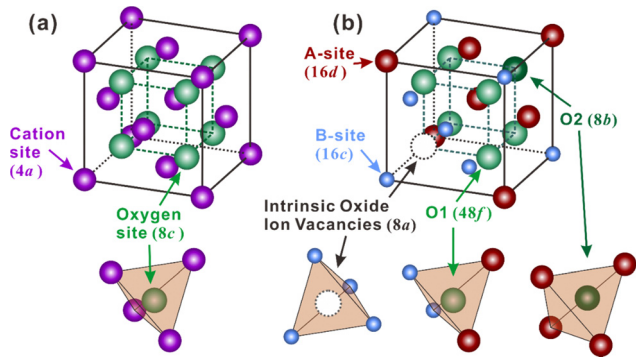

Fig. 1 (a) Fluorite and (b) pyrochlore crystal structures.

distributed. The pyrochlore structure, which takes an $A_2B_2O_7$ formula, is derived from the fluorite structure with both the cations and oxide ions arranged in order. A unit cell of the pyrochlore structure is composed of eight octants, one of which is shown in Fig. 1(b) to facilitate the explanation. Large cations occupy the A-site (16d), and small cations occupy the B-site (16c). Besides the intrinsic oxygen vacancies (8a site), there are two types of oxide ion sites; one is the 48f site in the center of tetrahedrons composed of two A and two B cations – named the O1 site hereafter – another is the 8b site in the center of tetrahedrons containing four A cations – named the O2 site hereafter.

The stability of the $A_2B_2O_7$ pyrochlore structure depends on the size of the A and B cations. A study from Minervini *et al.* using energy-minimization-based atomistic simulation calculations revealed that the ordering of the pyrochlore structure was enhanced with the increasing size of the A-site cations and decreasing size of the B-site cations.[10] Subramanian *et al.* reported a relationship between the structural ordering and the radius ratio of $r_{A^{3+}}/r_{B^{4+}}$,[11] and suggested a stable range of $1.46 < r_{A^{3+}}/r_{B^{4+}} < 1.8$ for the pyrochlore structure.[12] Blanchard *et al.*[13] and Yamamura *et al.*[14] conducted a combined study using X-ray absorption near edge structure (XANES) and X-ray diffraction (XRD) techniques to study the structure of $Ln_2Zr_2O_7$ (Ln = lanthanide elements), leading to the finding that when the Ln^{3+} cation is larger than Gd^{3+}, the samples take the pyrochlore structure, and when Ln^{3+} is smaller than Gd^{3+}, the fluorite structure is stable.[13] Moreover, a higher temperature appears to favor the structural disordering. Moriga *et al.* observed that $Gd_2Zr_2O_7$ had a pyrochlore structure between 1400 and 1900 °C, and a fluorite structure at higher temperature.[15] $Nd_2Zr_2O_7$ and $Sm_2Zr_2O_7$ undergo a phase transition from pyrochlore to fluorite at 2000 and 1530 °C, respectively.[16]

This review mainly focuses on the fluorite and pyrochlore-type proton conducting oxides attracting most of the interest, including acceptor-doped ZrO_2, CeO_2, $La_2Ce_2O_7$, and $La_2Zr_2O_7$. The progress of some other materials of lanthanide ziconates, stannates and titanates, and $La_2(Nb_{1-x}M_x)_2O_{7-\delta}$ (M = Y, Yb) – a recently discovered new proton conductor – was also summarized. Although nanocrystalline or porous ZrO_2 and CeO_2 are also known for their surface proton conduction at low temperature, detailed information can be found in a recent review paper,[17] and only the volume transport is discussed in this review paper.

2. Fluorite oxides

2.1 ZrO_2

Zirconia (ZrO_2) partly substituted by acceptor dopants is currently the most successful oxide ion-conducting electrolyte in

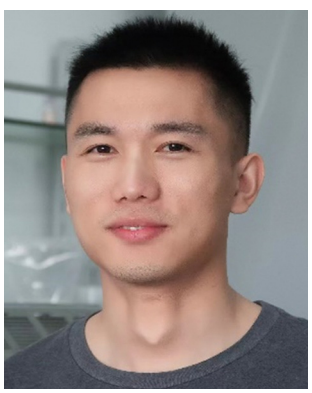

Shihang Guo

Shihang Guo is currently a PhD student at Soochow University. He received his Bachelor's degree (2016) from Anqing Normal University and his Master's degree (2019) from Nanjing Forestry University. His research interests mainly focus on the design of materials for oxygen electrodes and electrolytes in protonic ceramic electrochemical cells.

Lulu Jiang

Lulu Jiang is currently pursuing her PhD degree in new energy science and engineering at Soochow University. Her research interests mainly focus on the synthesis and characterization of electrolyte materials for protonic ceramic fuel cells (PCFCs). She is also investigating some novel oxide ion conducting electrolytes.

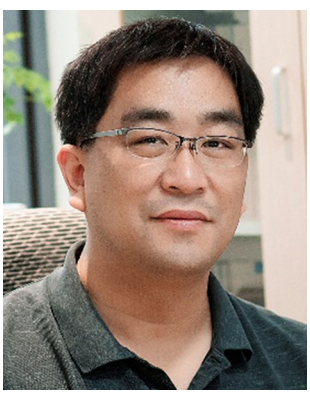

Donglin Han

Donglin Han obtained his Bachelor's (2005) and Master's degree (2007) at Tsinghua University, and PhD degree at Kyoto University (2011). He worked as a program-specific researcher, assistant professor and associate professor from 2011 to 2019 at Kyoto University. Then, he joined Soochow University as a full professor. His research is focused on ionic conducting oxide ceramics, especially proton conductors.

Open Access Article. Published on 08 September 2023. Downloaded on 6/11/2026 10:35:40 PM. This article is licensed under a Creative Commons Attribution 3.0 Unported Licence.

high temperature solid-state electrochemical devices, such as solid oxide fuel cells (SOFCs).[18,19] Pure ZrO_2 has a monoclinic structure between room temperature and 1170 °C, and becomes tetragonal between 1170 and 2370 °C. The cubic fluorite phase ZrO_2 exists between 2370 °C and the melting point (2830 °C).[20] Besides, pure ZrO_2 has no oxygen vacancy, asking for doping with lower valence elements to form oxygen vacancies and generate oxide ion conduction. Moreover, the temperature range for the cubic fluorite phase can be lowered by using appropriate doping strategies.[21] By doping 8–17 mol% Sc_2O_3, the temperature to form the cubic fluorite phase can be lowered to 1000 °C.[22] When Y (10–20 mol% Y_2O_3),[23] Gd (14–20 mol% Gd_2O_3)[24] and Sm (9–19 mol% Sm_2O_3)[25] are doped, the cubic fluorite phase can be stable even at room temperature.

Y-doped ZrO_2 – commonly known as yttria-stabilized zirconia (YSZ) – is the most widely used composition of doped ZrO_2, due to its excellent chemical stability and high oxide ion conductivity.[26–28] Replacing tetravalent Zr cations with trivalent Y cations results in the formation of oxygen vacancies following eqn (2) to preserve the electroneutrality:

$$2Zr_{Zr}^{\times} + Y_2O_3 + O_O^{\times} = 2ZrO_2 + 2Y_{Zr}^{'} + V_O^{\bullet\bullet} \quad (2)$$

YSZ has a cubic fluorite structure at a macroscopic level, but the larger size and lower valence state of Y^{3+} (1.019 Å) compared with those of Zr^{4+} (0.84 Å) induce local distortion resulting from the elastic and electrostatic interactions within the unit cell. Moreover, the oxygen vacancies activate not only the oxide ion conduction, but also the hydration reaction (eqn (1)). The presence of protons in YSZ was first reported by Stotz *et al.* in 1966.[29] In 1968, Wagner *et al.* reported a study on measuring the concentration and diffusivity of protons in YSZ at high temperature, and found that the concentration of protons was approximately 9.5×10^{-6} mol cm^{-3} at 1000 °C under p_{H_2O} = 1 atm.[30] Secondary ion mass spectrometry (SIMS), which is highly sensitive to hydrogen and its isotopes (*e.g.*, deuterium), is a powerful technique for measuring the proton concentration.[31–34] Sakai *et al.* used SIMS technology to probe the hydrated single crystal of 8 mol% Y_2O_3-doped ZrO_2 (8YSZ-SC), whose proton concentration was 6.8×10^{-8} mol cm^{-3} after annealing at 600 °C under p_{H_2O} = 0.02 atm.[35] Bay *et al.* reported the proton concentration of 1.7×10^{-6} mol cm^{-3} for 8YSZ-SC after annealing at 950 °C under p_{H_2O} = 0.066 atm.[36] Yamaguchi *et al.* improved the SIMS data analysis method, and tried to measure the proton concentration of 8YSZ-SC annealed at 600 °C under p_{H_2O} = 0.017 atm.[31] However, they found that the proton concentration was too low, below the SIMS detection limit ($\sim 1.7 \times 10^{-8}$ mol cm^{-3}). In 2018, Marinopoulos calculated the proton concentration in YSZ based on the formation energy of proton defects, and reported the value of 7.8×10^{-17} and 3.3×10^{-8} mol cm^{-3} at 227 and 927 °C, respectively.[37] They also simulated the migration paths of protons with migration barriers varying within 1.00–1.25 eV, higher than that in perovskite-type proton conductors like $SrTiO_3$ and $CaTiO_3$ (0.40–0.50 eV),[38] and $BaCeO_3$ and $BaZrO_3$ (0.42–0.83 eV).[39] Bay *et al.* further tested the performance of one-chamber fuel cells at 960 °C by using gold and platinum as the cathode and anode, respectively.[36] The results indicated that the maximum power density (P_{max}) of the one-chamber fuel cells using 17 at% Pr-doped 8YSZ as the electrolyte was 2.5 mW cm^{-2}, much higher than that using an 8YSZ electrolyte (0.1 mW cm^{-2}). The SIMS analysis detected higher deuterium ion intensity in 17% Pr-doped 8YSZ than that in 8YSZ, indicating that doping Pr improves the proton solubility, resulting in potentially increasing proton conductivity in the electrolyte. However, the enhanced performance may not only be due to the higher proton concentration. The improved cathodic effect of the electrolyte by doping Pr also improves the performance of fuel cells.

In addition, the solubility of protons in the intra-grain (bulk) and inter-grain (grain boundary) of YSZ appears to be different. The proton concentration of 8YSZ (8YSZ-poly) is higher than that of 8YSZ-SC under the same test conditions. After annealing at 600 °C under p_{H_2O} = 0.017 atm and at 950 °C under p_{H_2O} = 0.066 atm, the proton concentrations of 8YSZ-poly are 9.1×10^{-7} and 2.3×10^{-6} mol cm^{-3}, respectively, higher than those of the grain boundary-free single crystal 8YSZ (8YSZ-SC), implying that the proton concentration at the grain boundary of YSZ is higher than that in the bulk.

Dawson *et al.* investigated the crystal structure of YSZ and its potential as a proton-conducting material using combined classical and quantum mechanical computational techniques.[40,41] The redox stability of proton conductors is crucial as they must remain stable under both the oxidizing and reducing conditions. The reduction reaction involves the formation of oxygen vacancies which are compensated by electrons:

$$O_O^{\times} \rightarrow V_O^{\bullet\bullet} + \frac{1}{2}O_2 + 2e^{'} \quad (3)$$

In most cases, reaction (3) is accompanied by the reduction of metal cations. The reduction energy of undoped ZrO_2 is 5.47 eV, and decreases by doping Y. For 11 mol% Y_2O_3 doped ZrO_2, the reduction energy is 4.70 eV near Y^{3+} and 4.95 eV far away from Y^{3+}. Similarly, the hydration energy (reaction (1)) of undoped ZrO_2 is 6.48 eV, whereas that of 11 mol% Y_2O_3-doped ZrO_2 is 5.95 eV near Y^{3+} and 6.21 eV far away from Y^{3+}. Several proton conductors, including the oxides with fluorite, perovskite, or related structures, have reported hydration energies ranging from −3 to 1.5 eV.[42] However, the calculated hydration energy for ZrO_2 by Dawson *et al.* appears to be excessively high, suggesting that the hydration reaction may not occur. Besides, further investigation may also be necessary to evaluate the accuracy of the calculation results. Additionally, it was observed that the reduction energy and hydration energy decreased further with an increase in doping concentration.[41] These results indicate that doping Y^{3+} improves the hydration ability. Moreover, a trapping effect between the dopants and protons exists in the acceptor-doped ZrO_2, with the binding energy decreasing as the radius of the dopant increases, as shown in Fig. 2.

As aforementioned, the proton concentration of doped ZrO_2 is very low, in comparison with the concentration of oxygen vacancies. For example, the concentration of oxygen vacancies in 8YSZ is about 1.03×10^{-4} mol cm^{-3}, but its proton concentration reported in the literature varies within 10^{-6}–10^{-8} mol cm^{-3},[30,31,35,36]

© 2024 The Author(s). Published by the Royal Society of Chemistry

Open Access Article. Published on 08 September 2023. Downloaded on 6/11/2026 10:35:40 PM.
This article is licensed under a Creative Commons Attribution 3.0 Unported Licence.

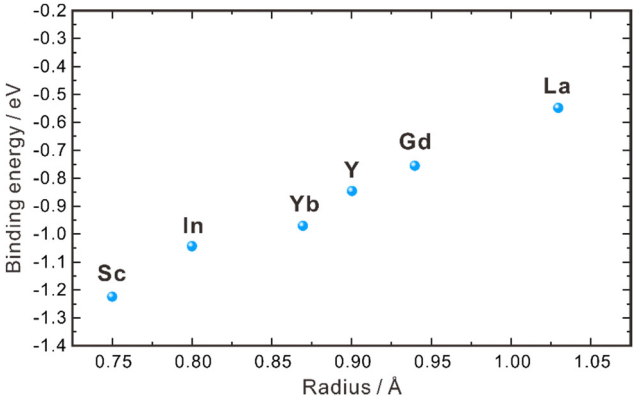

Fig. 2 Binding energies between dopants with different ionic radii and protons in the grain interior of ZrO_2.[40]

indicating that only a very limited amount of oxygen vacancies participates in the hydration reaction. Empirically, oxides with higher basicity favor the hydration reaction, facilitating the introduction of protons. However, ZrO_2 exhibits weak basicity,[43] resulting in only a small portion of oxygen vacancies participating in the hydration reaction. Furthermore, Bjørheim *et al.* discovered that among oxides with the same structure, the material with lower ionization potential (the difference between the valence band (VB) maximum and the vacuum level) exhibits a more negative hydration enthalpy.[42,44] In the case of ZrO_2, its ionization potential is approximately 6.86 eV,[45] indicating that the hydration reaction does not occur easily. This low proton concentration thereby leads to low proton conductivity. In 2004, Nigara *et al.* used the gas permeation method to measure the proton conductivity of 10 mol% Y_2O_3-doped ZrO_2 single crystal at 777–1527 °C, which was 1.5×10^{-8}–2.4×10^{-6} S cm^{-1}, far lower than the oxide ion conductivity.[46] Based on the results of both experimental investigations and theoretical calculations, it is clear that the proton concentration in the ZrO_2 system is low and the activation energy of proton diffusion is high. As a result, the bulk conductivity of protons is too low to give a significant contribution to the performance of the electrochemical devices using the ZrO_2-based electrolytes.

2.2 CeO_2

Ceria (CeO_2) has high thermal stability, and only undergoes phase transition to an orthorhombic α-$PbCl_2$ type structure (*Pnma*) under high pressure (*e.g.*, 31 GPa).[47,48] Doping low valence elements makes CeO_2 show high oxide ion conductivity, leading to the application of doped CeO_2 as an electrolyte for intermediate temperature solid oxide fuel cells (IT-SOFC).[22,49,50] Sm^{3+} was found to be one of the most effective dopants for CeO_2, and the conductivity of $Ce_{0.8}Sm_{0.2}O_{2-\delta}$ is as high as 1.0×10^{-2} S cm^{-1} at 500 °C.[51,52] Besides, some other dopants also impart CeO_2 with considerably high oxide ion conductivity at an intermediate temperature. For example, the conductivities of $Ce_{0.85}Gd_{0.15}O_{2-\delta}$ and $Ce_{0.95}La_{0.05}O_{2-\delta}$ at 500 °C are 3.0×10^{-3} and 4.2×10^{-3} S cm^{-1}, respectively.[53,54] In 1999, Doshi *et al.* fabricated a fuel cell with a 30 μm-thick $Gd_{0.2}Ce_{0.8}O_{2-\delta}$ electrolyte using a multilayer belt casting technique, showing P_{max} of 140 mW cm^{-2} at 450 °C.[55] Later, Ai *et al.* reported a fuel cell with a 15 μm-thick $Sm_{0.2}Ce_{0.8}O_{2-\delta}$ electrolyte deposited by a spin coating method, showing P_{max} of 103 mW cm^{-2} at 450 °C.[56]

The ionic conductivity in CeO_2 correlates with the oxygen vacancies, which are introduced by doping low valence elements. For example, the reaction of doping trivalent Sm is given as:

$$2Ce_{Ce}^{\times} + Sm_2O_3 + O_O^{\times} = 2CeO_2 + 2Sm_{Ce}^{'} + V_O^{\bullet\bullet} \quad (4)$$

The concentration of oxygen vacancies thereby increases with the increasing doping level. However, the relationship between the ionic conductivity of doped CeO_2 and dopant concentration is not simple. When the dopant concentration is low, the conductivity increases as the dopant concentration increases. However, when the dopant concentration is high, the conductivity decreases, due to the stronger local lattice distortion or the trapping effect between negatively charged dopants and positively charged oxygen vacancies. The solubility varies for different dopants in the cubic CeO_2 phase. For Sm and Y-doped CeO_2 prepared using the Pechini sol–gel method and heated at 900 °C, the crystal structure is cubic fluorite when the concentrations of Sm and Y are below 31.3 and 28 at%, respectively.[57,58] For Gd-doped CeO_2 prepared with the solid-state reaction method and annealed at 1400 °C, the cubic fluorite phase can be obtained with a Gd concentration below 20 at%.[59] When the doping level exceeds the limits for the cubic fluorite phase, a C-type structure ($Ia\bar{3}$) phase forms.[57,58,60,61] The C-type structure can be described as a cubic fluorite superstructure resulted from the ordering of vacancies in the anion sub-lattice, and is commonly seen for rare earth oxides. This structure is also known as a double fluorite structure, and the lattice constant is twice as large as that of a simple fluorite one.[8,16]

CeO_2 allows higher acceptor solubility, leading to the presence of a significant number of oxygen vacancies. Nevertheless, the high stability of these vacancies makes it challenging to hydrate and introduce protons, resulting in a low concentration of protons.[44] In 1999, Sakai *et al.* utilized the SIMS method to determine the proton concentration of pure polycrystalline CeO_2 and that doped with rare earth elements ($Ce_{0.8}M_{0.2}O_{2-\delta}$, M = Y, La, Nd, Sm, Gd, Yb), which were annealed at 880 and 990 °C under p_{H_2O} = 0.03 atm, as shown in Fig. 3.[62] The proton concentration of pure CeO_2 is low ($\sim 1.7 \times 10^{-6}$ mol cm^{-3}) and increases by 10–100 times by doping the trivalent rare earth elements. From Fig. 3, one can see that the proton concentration decreases with increasing lattice constants of $Ce_{0.8}M_{0.2}O_{2-\delta}$ containing larger dopants. By doping the smallest dopant Yb, the highest proton concentration of 3.3×10^{-4} mol cm^{-3} was obtained at 990 °C, while doping the largest La leads to the lowest proton concentration of 1.2×10^{-5} mol cm^{-3}.[62] The reason is not clear, but enhanced mismatch between the size of dopants and host cations (Ce^{4+}) may hamper the hydration reaction. It should be noted that the proton concentration of all the aforementioned doped CeO_2 is higher than that of the single crystal 8YSZ (namely, 8YSZ-SC),[36] and $Ce_{0.8}Yb_{0.2}O_{2-\delta}$ has a proton

Open Access Article. Published on 08 September 2023. Downloaded on 6/11/2026 10:35:40 PM.
This article is licensed under a Creative Commons Attribution 3.0 Unported Licence.

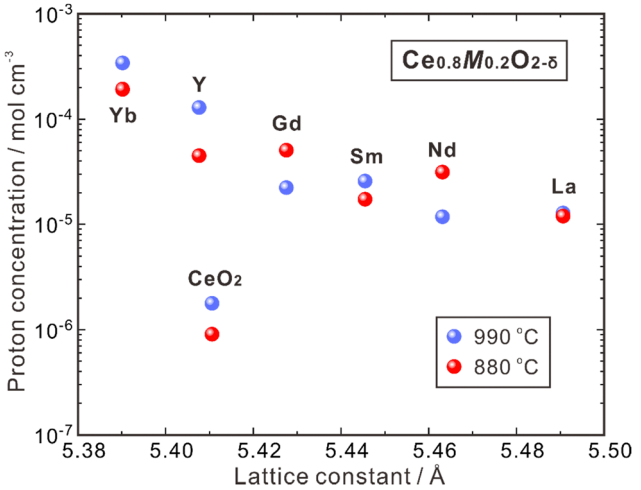

Fig. 3 Proton concentration in undoped CeO_2 and $Ce_{0.8}M_{0.2}O_{2-\delta}$ (M = Y, La, Nd, Sm, Gd, Yb) after annealing at 880 and 990 °C in a wet atmosphere (p_{H_2O} = 0.03 atm).[62]

concentration two orders of magnitude higher than that of 8YSZ-SC, attributed possibly to the difference in thermodynamic and chemical properties of the defects.[63]

In a reducing atmosphere, CeO_2 exhibits electron conduction as Ce^{4+} is reduced to Ce^{3+},[28,64] leading to the ability of CeO_2 to permeate hydrogen when protons conduct simultaneously. Nigara *et al.* studied the permeability of hydrogen in pure and doped CeO_2 at high temperatures, and confirmed the presence of proton conductivity.[65–68] Assuming that hydrogen atoms are dissociated into protons and electrons, the proton conductivity can be roughly calculated based on the gradient of chemical potential of hydrogen. The proton conductivity of undoped CeO_2 is 8.5×10^{-6} S cm^{-1} at 1050 K, which increases to 1.6×10^{-4} S cm^{-1} at 1800 K.[65] The proton conductivity of $Ce_{0.9}Gd_{0.1}O_{2-\delta}$ is 1.2×10^{-6} S cm^{-1} at 1070 K, and increases to 1.4×10^{-4} S cm^{-1} at 1800 K.[66] The proton conductivity of $Ce_{0.8}Yb_{0.2}O_{2-\delta}$ is 1.0×10^{-6} S cm^{-1} at 1000 K, and increases to 1.0×10^{-4} S cm^{-1} at 1800 K.[67] Among the compositions studied, $Ce_{0.85}Ca_{0.15}O_{2-\delta}$ shows the highest proton conductivity, which is 1.4×10^{-6} and 5.0×10^{-5} S cm^{-1} at 1050 and 1800 K, respectively.[68] The permeability of hydrogen is not solely determined by proton conductivity, but is also influenced by electronic conductivity. Therefore, the estimation of proton conductivity using hydrogen permeability can only be a rough approximation.

Although proton incorporation and conduction were confirmed in both pure and doped CeO_2 at high temperatures, the proton conductivity is quite low, far lower than the required level ($\sim$0.01 S cm^{-1}) for application as a proton-conducting electrolyte. Therefore, similar to the case of doped ZrO_2, the application of doped CeO_2 as the electrolyte is mainly based on its oxide ion conduction, and the contribution from volume proton conduction is negligibly small.

2.3 $La_2Ce_2O_7$

CeO_2 doped with lanthanide elements exhibits a sharp decline in oxide ion conductivity as doping levels rise over 10–20 mol%,[69–71] but CeO_2 heavily doped with some large lanthanides (*e.g.*, La) can be hydrated and exhibits proton conduction in wet atmospheres.[72] 50 at% La-doped CeO_2 – namely $Ce_{0.5}La_{0.5}O_{2-\delta}$, and is generally depicted in the literature as $La_2Ce_2O_7$ – takes a disordered fluorite structure and has high oxide ion conductivity and moderate proton conductivity, depending on the temperature and atmosphere. Kalland *et al.* measured water uptake and hydration enthalpy in $La_2Ce_2O_7$ using combined thermogravimetry (TG) and differential scanning calorimetry (DSC) techniques,[73] and determined the change of standard hydration enthalpy ($\Delta_{hydr}H^\circ$) of -74 kJ mol^{-1}, which was independent on the water uptake. They also prepared the solid solution of $(La_{1-x}Nd_x)_2Zr_2O_{7-\delta}$ with $La_2Ce_2O_7$ and $Nd_2Ce_2O_7$ as the end compositions and found that the water uptake increased with the increasing La concentration. They thereby proposed a model explaining that in $La_2Ce_2O_7$, the oxide ions and oxygen vacancies coordinated with four La^{3+} cations have the strongest hydration ability, and those coordinated with less La^{3+} cations are less prone to be hydrated.[73] Ismail *et al.* recently reported that both the proton concentration and conductivity increased by doping divalent alkaline earth elements to replace La and trivalent earth elements to replace Ce. Besides the increasing oxygen vacancies by these doping strategies, which benefits the hydration reaction, another reason is suggested to be the formation of new coordination types, including the oxide ions and oxygen vacancies coordinated with three La^{3+} and one A^{2+} (A = Ca, Sr and Ba) cations,[74] and three La^{3+} and one B^{3+} (B = Y, Ho, Er, Tm and Yb) cations.[75] Following the model proposed by Kalland *et al.*, these new coordination types containing lower valence dopants benefit the hydration reaction, leading to higher proton concentration and conductivity.[73–75] It should be noted that increasing the concentration of oxygen vacancies is the strategy commonly taken to increase the proton conductivity, but the model proposed by Kalland *et al.* in the $La_2Ce_2O_7$ system emphasizes the importance to pay attention on the coordination environment surrounding the oxide ions and oxygen vacancies.

$La_2Ce_2O_7$ is, in most conditions, a mixed conductor with protons and oxide ions as the ionic charge carriers, and also shows partial electron conduction in a reducing atmosphere, due to the reduction of a part of Ce^{4+} to Ce^{3+}.[69,74] Sun *et al.* studied the effect of p_{H_2O} and temperature on the conduction behavior of $La_2Ce_2O_7$, and found that the total conductivity increased significantly with increasing p_{H_2O}, due to the enhancement in proton conduction, as shown in Fig. 4(a).[76] For example, the proton conductivity (σ_{H^+}) of $La_2Ce_2O_7$ increases from 2.44×10^{-5} S cm^{-1} to 6.68×10^{-5} S cm^{-1} with p_{H_2O} increasing from 0.0025 atm to 0.03 atm at 550 °C, and the transport number of protons (t_{H^+}) – reflecting the contribution of proton conduction to the total conduction – also increases. Since higher temperature activates the oxide ion conduction and promotes dehydration, t_{H^+} decreases with the elevating temperature. t_{H^+} of $La_2Ce_2O_7$ is 0.90 at 250 °C under p_{H_2O} = 0.03 atm, and decreases to 0.13 at 550 °C.[76] Therefore, the contribution of proton conduction in pristine $La_2Ce_2O_7$ at the intermediate temperature range (450–700 °C) is quite small. Later on, Ismail *et al.* doped trivalent rare earth elements

© 2024 The Author(s). Published by the Royal Society of Chemistry

Open Access Article. Published on 08 September 2023. Downloaded on 6/11/2026 10:35:40 PM.
This article is licensed under a Creative Commons Attribution 3.0 Unported Licence.

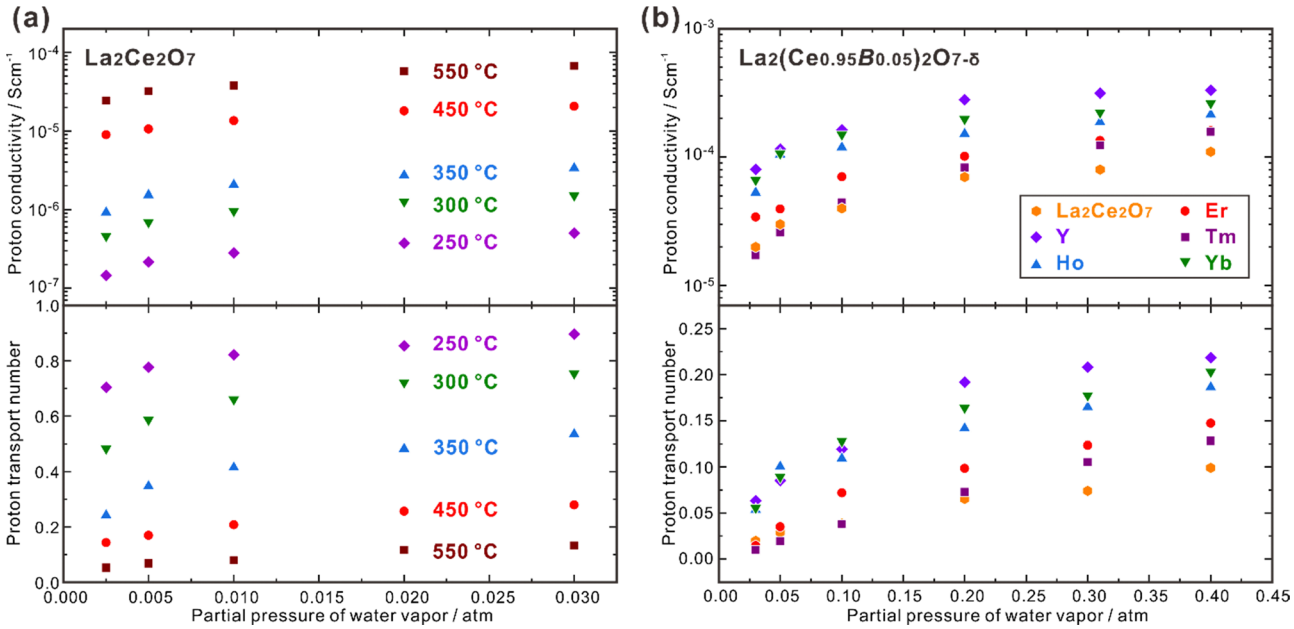

Fig. 4 Proton conductivity and proton transport number of (a) $La_2Ce_2O_7$ in wet air,[76] and (b) $La_2(Ce_{0.95}B_{0.05})_2O_{7-\delta}$ (B = Y, Ho, Er, Tm and Yb) at 600 °C in wet oxygen plotted against p_{H_2O}.[75]

(Y, Ho, Er, Tm and Yb) to substitute Ce and studied the conduction behavior in the atmosphere with p_{H_2O} varying within 0.03–0.40 atm.[75] Among the compositions studied, they found that $La_2(Ce_{0.95}Y_{0.05})_2O_{7-\delta}$ showed the highest σ_{H^+}, which was 8.0×10^{-5} S cm^{-1} at 600 °C under p_{H_2O} = 0.03 atm, four times higher than that of pristine $La_2Ce_2O_7$ (2.0×10^{-5} S cm^{-1}), as shown in Fig. 4(b).[75] Moreover, by increasing p_{H_2O} to 0.40 atm, σ_{H^+} of $La_2(Ce_{0.95}Y_{0.05})_2O_{7-\delta}$ further increased by more than four times to 3.3×10^{-4} S cm^{-1}, and t_{H^+} was kept at a moderate value of 0.22.[75] These results indicate that by optimizing the composition and environmental atmosphere (*e.g.*, increasing p_{H_2O}), the proton conduction in $La_2Ce_2O_7$ can be enhanced efficiently. However, it should be noted that the majority charge carriers in $La_2Ce_2O_7$ in the intermediate temperature range are oxide ions, and t_{H^+} is much smaller than $t_{O^{2-}}$. Therefore, the fuel cells and electrolyzers using the $La_2Ce_2O_7$-based electrolytes should not be classified into the category of protonic ceramic electrochemical devices.

3. Pyrochlore oxides

3.1 $La_2Zr_2O_7$

As a pyrochlore-type proton conductor, lanthanum zirconate ($La_2Zr_2O_7$) attracts a lot of interest and has been studied profoundly. Pristine $La_2Zr_2O_7$ has low electrical conductivity (*e.g.*, 1.0×10^{-5} S cm^{-1} in a humidified H_2 atmosphere at 900 °C),[77] so it is commonly doped with acceptor dopants to increase the concentration of oxygen vacancies, which is beneficial for both the proton and oxide ion conduction. In this section, a summarization of the information of the solubility of dopants, electrical conduction behavior, and conduction mechanism of protons in the crystal structure of $La_2Zr_2O_7$ is provided.

3.1.1 Dopants. To improve the conduction behavior, low valence dopants are introduced into the La or Zr-sites to generate oxygen vacancies, which play a crucial role in the conduction of both oxide ions and protons. Divalent alkaline earth elements (*e.g.*, Ca, Sr) are commonly used to substitute La. Interestingly, the method for sample preparation affects the solubility of the dopants in $La_2Zr_2O_7$ significantly. Omata *et al.* found that the doping limit of Sr was x = 0.01 in $(La_{1-x}Sr_x)_2Zr_2O_{7-\delta}$, which was prepared with a solid-state reaction method and sintered at 1550 °C.[78] Huo *et al.* found that the Sr doping limit was x = 0.025 by using an oxalic acid co-precipitation method and sintering at 1500 °C.[79] Antonova *et al.* reported a higher Sr doping limit of x = 0.035 when the sintering was performed at 1600 °C on the samples prepared with a citrate–nitrate method.[80] These results clearly indicate that by using the method to synthesize the materials with smaller grain size and sintering at higher temperature, the solubility of Sr in $La_2Zr_2O_7$ is improved. This is reasonable, since the inter-diffusion of elements between raw materials will be improved by decreasing the diffusion distance (grain size) and thermally activated. Furthermore, using wet processes for synthesis benefits the homogeneous mixing of the raw materials. The doping limits of Ca in $La_2Zr_2O_7$ shows similar correlation with the method for sample preparation. Omata *et al.* found the doping limit of Ca to be x = 0.025 in $(La_{1-x}Ca_x)_2Zr_2O_{7-\delta}$ which was sintered at 1550 °C using the solid-state reaction method.[81] Islam *et al.* reported a higher doping limit of x = 0.035 using a combustion synthesis technique by sintering at 1400 °C.[82] Antonova *et al.* found an even higher doping limit of x = 0.05 when the sample was prepared by the citrate-nitrate method and the sintering was conducted at 1600 °C.[83]

In addition, the Zr-site can also be used for doping trivalent rare earth elements (*e.g.*, Y, Nd, Sm, Gd) and divalent alkaline

Open Access Article. Published on 08 September 2023. Downloaded on 6/11/2026 10:35:40 PM. This article is licensed under a Creative Commons Attribution 3.0 Unported Licence.

earth elements (*e.g.*, Ca) to introduce oxygen vacancies. Omata *et al.* prepared $La_2(Zr_{1-y}Ca_y)_2O_{7-\delta}$ with the doping limit of Y to be $y = 0.0075$.[81] Han *et al.* found that the doping limit of Y in $La_2(Zr_{1-y}Y_y)_2O_{7-\delta}$ reached above $y = 0.15$ using the solid state reaction method, but the doping limits of Nd, Sm and Gd elements were only around $y = 0.05$.[84]

3.1.2 Hydration. Increasing the dopant concentration leads to the generation of more oxygen vacancies, benefiting the hydration reaction (eqn (1)) to increase the concentration of protons. Omata *et al.* measured the proton concentration in $La_2Zr_2O_7$ doped with alkaline earth elements by counting the amount of thermally desorbed water using a quadrupole mass spectrometer.[78,85] The samples were annealed in wet O_2 ($p_{H_2O} \sim 0.30$ atm) at 800 °C for 12 h for hydration, leading to the measured proton concentration of 7.1×10^{-7} mol cm^{-3} for $La_2Zr_2O_7$, which increases to 3.9×10^{-5} mol cm^{-3} and 7.9×10^{-5} mol cm^{-3} for $(La_{0.975}Ca_{0.025})_2Zr_2O_{7-\delta}$ and $(La_{0.96}Ca_{0.04})_2Zr_2O_{7-\delta}$, respectively. Antonova *et al.* used TG analysis to measure the proton concentration in $(La_{0.975}Ca_{0.025})_2Zr_2O_{7-\delta}$ and $(La_{0.95}Ca_{0.05})_2Zr_2O_{7-\delta}$ which were hydrated by cooling from 950 °C to 300 °C at 60 °C h^{-1} in wet O_2 ($p_{H_2O} \sim 0.24$ atm).[83,86] The proton concentrations are 7.4×10^{-5} and 1.1×10^{-4} mol cm^{-3} for $(La_{0.975}Ca_{0.025})_2Zr_2O_{7-\delta}$ and $(La_{0.95}Ca_{0.05})_2Zr_2O_{7-\delta}$, respectively. These results indicate that doping divalent Ca into the La-site is effective in increasing the proton concentration in $La_2Zr_2O_7$. Other alkaline earth elements show similar effect on improving the hydration ability of $La_2Zr_2O_7$, but the proton concentration in the Mg-doped samples is much lower than those doped with Ca and Sr.[78] The large difference in ionic radius between Mg^{2+} (0.890 Å) and La^{3+} (1.160 Å) can result in large lattice distortion, which is not favorable for hydration reactions.

Furthermore, the difference in doping the same dopants into the La and Zr-sites was compared. The proton concentration in $(La_{0.99}Sr_{0.01})_2Zr_2O_{7-\delta}$ annealed at 800 °C under $p_{H_2O} \sim 0.30$ atm was reported to be 2.0×10^{-5} mol cm^{-3}, higher than that in $La_2(Zr_{0.99}Sr_{0.01})_2O_{7-\delta}$ (1.5×10^{-5} mol cm^{-3}).[78] Omata *et al.* suggested that oxygen vacancies form in the 48f and 8b sites, when doping into the La-site, and only form in the 48f site, when doping into the Zr-site.[85] The authors speculated that the oxygen vacancies in different sites resulted in the differences in hydration ability to introduce protons with different mobilities.[85] However, theoretical calculations indicate that oxygen vacancies mainly formed at the 48f site in $La_2Zr_2O_7$ by acceptor-doping and are energetically unfavorable in the 8b site.[87–91] The appropriateness of the aforementioned viewpoint needs further verification. We suggest that the discrepancy is due to the fact that the eight-coordinated radius of Ca^{2+} (1.120 Å[11]) is closer to that of La^{3+} (1.160 Å[11]), but the six-coordinated radius of Ca^{2+} (1.000 Å[11]) is obviously larger than that of Zr^{4+} (0. 720 Å[11]). This mismatch in cation radii induces local distortions, which is unfavorable for the hydration reaction.

Interestingly, it seems that not all the oxygen vacancies generated by doping participate the hydration reaction. Björketun *et al.* reported that only 59% of the oxygen vacancies in $(La_{0.975}Ca_{0.025})_2Zr_2O_{7-\delta}$ and $(La_{0.955}Ca_{0.045})_2Zr_2O_{7-\delta}$ participated into the hydration reaction.[88] Omata *et al.* found that the ratio of hydratable oxygen vacancies in $(La_{0.975}Ca_{0.025})_2Zr_2O_{7-\delta}$ and $(La_{0.96}Ca_{0.04})_2Zr_2O_{7-\delta}$ were 30%[78] and 38%,[85] respectively. Antonova *et al.* reported that 36%[83] and 45%[86] of the oxygen vacancies in $(La_{0.975}Ca_{0.025})_2Zr_2O_{7-\delta}$ and $(La_{0.95}Ca_{0.05})_2Zr_2O_{7-\delta}$, respectively, were active for the hydration reaction. The reason is still unclear, but a possible explanation is that the hydration ability of the oxygen vacancies and oxide ions strongly depends on their coordination environment. Analogous to the case in the $La_2Ce_2O_7$, the oxygen vacancies and oxide ions surrounded by trivalent La and the dopants with lower valence might be prone to participate into the hydration reaction, and those in the vicinity of tetravalent cations (Ce^{4+}, Zr^{4+}) are difficult to be hydrated, making the system unable to be fully hydrated.

3.1.3 Conduction behavior. The proton conductivity of $(La_{1-x}Ca_x)_2Zr_2O_{7-\delta}$ increases with the increasing Ca concentration.[81,92] The increasing proton concentration appears to be the main reason, since there is a negligibly small difference in the mobility of protons between $(La_{2-x}Ca_x)Zr_2O_{7-\delta}$ with different Ca concentrations.[92] Generally speaking, the mobility of protons decreases with the increasing dopant concentration as the negatively charged acceptor dopants interact with positively charged protons, resulting in a trapping effect of protons by the dopants. However, the mobilities of protons in $(La_{1-x}Ca_x)_2Zr_2O_{7-\delta}$ with different Ca concentrations are very close, revealing a trapping effect that is independent of Ca dopant concentration.

Besides, the site for doping was also suggested to play an effective role in influencing the proton concentration and conductivity. Omata *et al.* found that $(La_{0.96}Ca_{0.04})_2Zr_2O_{7-\delta}$ has a proton concentration about three times higher than that in $La_2(Zr_{0.98}Ca_{0.02})_2O_{7-\delta}$, although these two samples have the same concentration of extrinsic oxygen vacancies ($\delta = 0.04$).[85] They further separated the partial conductivities of protons and oxide ions in $(La_{0.975}Ca_{0.025})_2Zr_2O_{7-\delta}$ and $La_2(Zr_{0.9925}Ca_{0.0075})_2O_{7-\delta}$, and found that as shown in Fig. 5, the proton conductivity of $(La_{0.975}Ca_{0.025})_2Zr_2O_{7-\delta}$ (6.8×10^{-4} S cm^{-1}) is nearly 7 times higher than that of $La_2(Zr_{0.9925}Ca_{0.0075})_2O_{7-\delta}$ (1.0×10^{-4} S cm^{-1}) at 600 °C, although the concentration of oxygen vacancies in $(La_{0.975}Ca_{0.025})_2Zr_2O_{7-\delta}$ ($\delta = 0.025$) is less than twice as high as that in $La_2(Zr_{0.9925}Ca_{0.0075})_2O_{7-\delta}$ ($\delta = 0.015$).[85] The proton conductivity in $(La_{0.985}Ca_{0.015})_2Zr_2O_{7-\delta}$, which has the same concentration of oxygen vacancies as $La_2(Zr_{0.9925}Ca_{0.0075})_2O_{7-\delta}$, is 3.9×10^{-4} S cm^{-1} at 600 °C.[85]

As shown in Fig. 5, when the temperature is not high enough (typically < 600 °C), Ca-doped $La_2Zr_2O_7$ is almost a pure proton conductor in wet H_2, since the partial conductivity of protons is higher by more than one order of magnitude than that of oxide ions. However, with the increasing temperature, the proton conductivity decreases due to dehydration, and the contribution from oxide ions increases. In the case of $(La_{0.975}Ca_{0.025})_2Zr_2O_{7-\delta}$, when the temperature is around 835 °C, the partial conductivities of protons and oxide ions are close. When the temperature is elevated to 900 °C, the partial conductivity of oxide ions is higher than that of protons by one order of magnitude, making the material become nearly a pure oxide ion conductor.

© 2024 The Author(s). Published by the Royal Society of Chemistry

Open Access Article. Published on 08 September 2023. Downloaded on 6/11/2026 10:35:40 PM.
This article is licensed under a Creative Commons Attribution 3.0 Unported Licence.

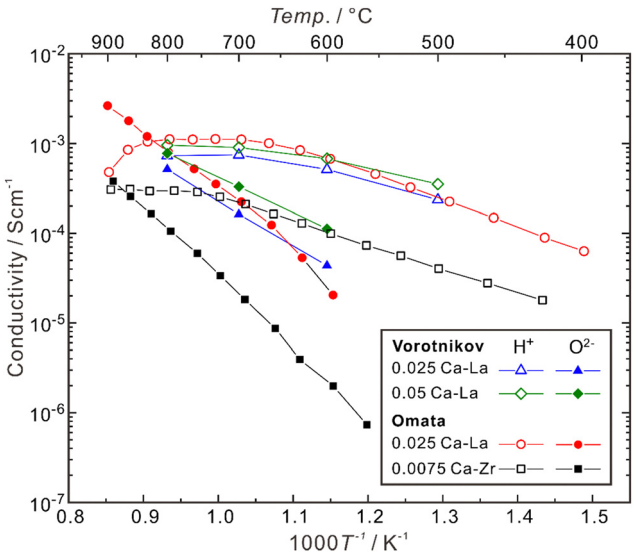

Fig. 5 Temperature dependence of partial conductivities of proton, oxide ion in $(La_{0.975}Ca_{0.025})_2Zr_2O_{7-\delta}$ (0.025 Ca–La) and $(La_{0.95}Ca_{0.05})_2Zr_2O_{7-\delta}$ (0.052 Ca–La) in wet H_2 (p_{H_2O} ~ 0.028 atm),[92] and $(La_{0.975}Ca_{0.025})_2Zr_2O_{7-\delta}$ (0.025 Ca–La) and (b) $La_2(Zr_{0.9925}Ca_{0.0075})_2O_{7-\delta}$ (0.0075 Ca–Zr) in wet H_2 (p_{H_2O}: 0.017–0.25 atm).[81] The samples are polycrystalline, and the conductivities comprise the contributions from both bulk (intra-grain) and grain boundaries (inter-grain).

Besides doping alkaline earth elements, substituting Zr with trivalent rare earth elements (*e.g.*, Y) also effectively enhances the proton conduction. Y^{3+} has the same valence state as La^{3+} and cannot be used as an acceptor dopant for the A-site. However, doping at the tetravalent B-site can introduce oxygen vacancies, which in turn increases the concentration and partial conductivity of protons. Labrincha *et al.* reported that $La_2Zr_2O_7$ and $La_2(Zr_{0.84}Y_{0.16})_2O_{7-\delta}$ exhibited proton conduction at temperatures lower than 1000 °C,[93] and the conductivities at 900 °C were 3.3×10^{-5} and 1.0×10^{-4} S cm^{-1} for $La_2Zr_2O_7$ and $La_2(Zr_{0.84}Y_{0.16})_2O_{7-\delta}$, respectively. Shimura *et al.* measured the conduction behavior of $La_2(Zr_{0.9}Y_{0.1})_2O_{7-\delta}$, whose t_{H^+} was 0.45 and 0.10 at 600 and 900 °C, respectively, corresponding to σ_{H^+} of 1.1×10^{-4} and 1.5×10^{-4} S cm^{-1}, respectively.[77] Han *et al.* measured the conductivities of $La_2Zr_2O_7$ doped with various concentrations of Y, and found that the bulk conductivity of $La_2(Zr_{0.9}Y_{0.1})_2O_{7-\delta}$ was 3.68×10^{-4} S cm^{-1} at 600 °C in wet H_2, which was the highest among the compositions studied in their work.[84]

3.1.4 Conduction mechanism of protons. Stable sites and conduction route of protons in $La_2Zr_2O_7$ have been studied by theoretical calculation.[88,90] Besides the viewpoint of anion-centered tetrahedrons as shown in Fig. 1(b), the pyrochlore structure can also be viewed as a connection of cation-centered octahedrons. In the case of $La_2Zr_2O_7$, six O1 anions coordinate a Zr cation to form a ZrO_6 octahedron, which links adjacent ZrO_6 octahedrons by sharing the apical O1 anions, as shown in Fig. 6(a). However, the O2 anions are relatively isolated and do not belong to any ZrO_6 octahedrons. Toyoura *et al.* found that there are two and four equivalent stable proton positions around the O1 and O2 anions, respectively, but the energy of the protons around the O2 anions are 1.2 eV higher than that around the O1 anions.[90] Three basic motions of protons – path 1, 2 and 3 in Fig. 6(b) – were further separated. Path 1 is a short-range hopping path (0.95 Å) connecting three adjacent H1 sites forming an equilateral triangle. Path 2 is a partial rotation around the O1 ion with the migration distance of 2.28 Å. However, paths 1 and 2 can only make protons migrating in closed regions, and path 3 which connects the closed regions is the key path promoting protons to migrate a long distance (3.09 Å). The energy barriers of paths 1 (0.32 eV) and 3 (0.39 eV) are lower than that of path 2 (0.54 eV), so the migration of protons in the pyrochlore structure of $La_2Zr_2O_7$ can be realized by paths 1 and 3.[90] Toyoura *et al.* further simulated the influence of acceptor dopants on the proton conduction, and found that diffusion coefficients decreased by doping divalent cations of alkaline earth elements (Mg, Ca, Sr and Ba) to partly replace La or Zr, or trivalent Y to replace Zr, due to the association between protons and the negatively charged dopants relative to the host cations of La(III) and Zr(IV). Interestingly, if assuming that the extrinsic oxygen vacancies formed by acceptor-doping contribute to the hydration reaction significantly, high proton conductivity can be expected. For example, assuming that 32.5% of the extrinsic oxygen vacancies in $La_2(Zr_{0.9}Y_{0.1})_2O_{7-\delta}$ (δ = 0.1), the proton concentration will be 0.065 per $La_2(Zr_{0.9}Y_{0.1})_2O_{7-\delta}$ formula unit, and the proton conductivity is predicted to be around 0.01 S cm^{-1} at 600 °C.[84] However, the experimentally measured value is only 3.68×10^{-4} S cm^{-1}, far lower than the prediction.[84] Low hydration ability of the sample is the major reason, since only 3.5% of the extrinsic oxygen vacancies participate in the hydration reaction and the proton concentration is as low as 0.007 per formula unit.[84] In order to increase the proton conductivity of the $La_2Zr_2O_7$-based material, the hydration ability needs to be enhanced.

3.2 $La_2(Nb_{1-x}M_x)_2O_{7-\delta}$

$La_2(Nb_{1-x}M_x)_2O_{7-\delta}$ (M = rare earth elements) is a new class of fluorite/pyrochlore proton conductor. Although it contains neither Zr nor Ce, the idea of this composition was inspired from $La_2Zr_2O_7$. The design strategy of $La_2(Nb_{1-x}M_x)_2O_{7-\delta}$ is to use a mixture of pentavalent Nb and trivalent rare earth elements (M) to occupy the tetravalent B-site. When the atomic ratio between Nb and rare earth elements is 1 : 1, the average positive charge of the B-site is four. Furthermore, interestingly, if the ratio between Nb and rare earth elements is increased over unity, oxygen vacancies form following

$$2Nb_B^{\bullet} + M_2O_3 + 2O_O^{\times} = 2M_B^{'} + Nb_2O_5 + 2V_O^{\bullet\bullet} \quad (5)$$

where $Nb_B^{\bullet}$ and $M_B^{'}$ are the Nb and rare earth cations occupying the B-site. Therefore, by simply changing the concentration of the domestic cations in the B-site, oxygen vacancies can be created, favoring the hydration reaction. Firstly, dopant candidates of rare earth elements were screened, including Sc, Y, Nd, Sm, Gd, Ho, Er, Tm and Yb, but only limited compositions showed single phase: $La_2(Nb_{0.5}Sc_{0.5})_2O_{7-\delta}$, $La_2(Nb_{1-x}Y_x)_2O_{7-\delta}$

Open Access Article. Published on 08 September 2023. Downloaded on 6/11/2026 10:35:40 PM.
This article is licensed under a Creative Commons Attribution 3.0 Unported Licence.

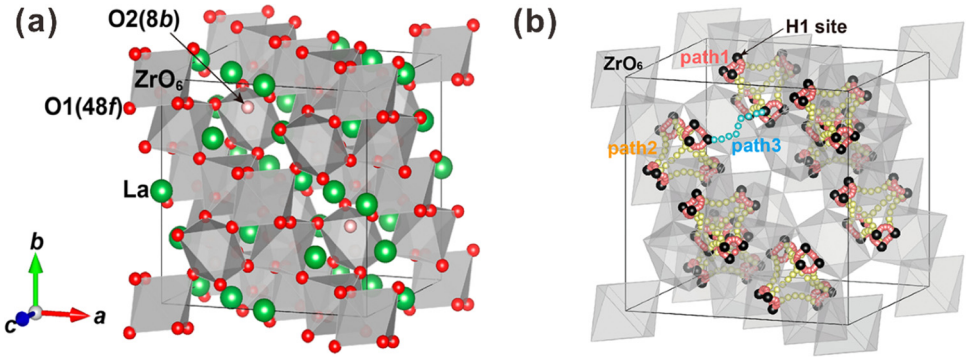

Fig. 6 (a) Pyrochlore crystal structure of $La_2Zr_2O_7$, where the green and red balls are La and O ions, and the grey octahedrons are ZrO_6 units. (b) Conduction route of protons in $La_2Zr_2O_7$. Reprinted with permission,[90] Copyright [2015] American Chemical Society.

(LNY, x = 0.60, 0.65, 0.70),[94] and $La_2(Nb_{0.45}Yb_{0.55})_2O_{7-\delta}$ (LNYb55).[95] Since there are no extrinsic oxygen vacancies in $La_2(Nb_{0.5}Sc_{0.5})_2O_{7-\delta}$, the conductivity of this sample showed no response to moisture, indicating that there is no proton conduction. The crystal structure of $La_2(Nb_{1-x}Y_x)_2O_{7-\delta}$ (LNY) depends on the composition, and is pyrochlore and fluorite,

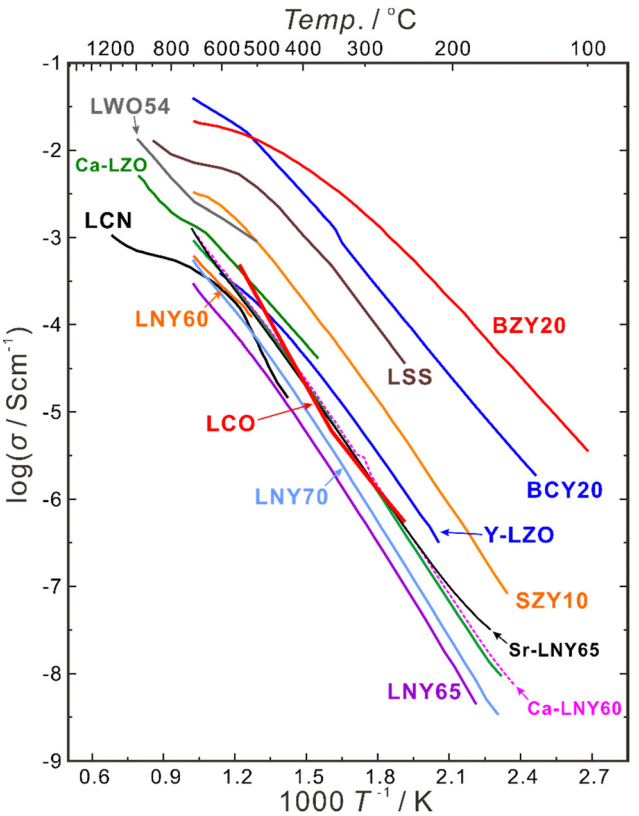

Fig. 7 Total conductivities of $BaZr_{0.8}Y_{0.2}O_{3-\delta}$ (BZY20),[94] $BaCe_{0.8}Y_{0.2}O_{3-\delta}$ (BCY20),[94] $SrZr_{0.9}Y_{0.1}O_{3-\delta}$ (SZY10),[94] $La_2(Zr_{0.9}Y_{0.1})_2O_{7-\delta}$ (Y-LZO),[84] $La_2(Nb_{0.40}Y_{0.60})_2O_{7-\delta}$ (LNY60),[94] $La_2(Nb_{0.35}Y_{0.65})_2O_{7-\delta}$ (LNY65),[94] $La_2(Nb_{0.30}Y_{0.70})_2O_{7-\delta}$ (LNY70),[94] $(La_{0.95}Ca_{0.05})_2(Nb_{0.40}Y_{0.60})_2O_{7-\delta}$ (Ca-LNY60),[96] $(La_{0.95}Sr_{0.05})_2(Nb_{0.35}Y_{0.65})_2O_{7-\delta}$ (Sr-LNY65)[96] in wet H_2 (p_{H_2O} = 0.05 atm), $(La_{0.975}Ca_{0.025})_2Zr_2O_{7-\delta}$ (Ca-LZO) in wet H_2 (p_{H_2O} ~ 0.02 atm),[81] $La_2Ce_2O_7$ in wet air (p_{H_2O} = 0.03 atm),[76] $La_{0.9}Sr_{0.1}ScO_{3-\delta}$ (LSS) in wet Ar-1% H_2 (p_{H_2O} = 0.02 atm),[97] $La_{27}W_5O_{54+\delta}$ (LWO54) in wet Ar-5% H_2O (p_{H_2O} ~ 0.025 atm),[98] and $La_{0.99}Ca_{0.01}NbO_{4-\delta}$ (LCN) in wet H_2 (p_{H_2O} ~ 0.02 atm).[99]

when x = 0.60 and 0.65 and x = 0.70, respectively.[94] A clear H_2O/D_2O isotope effect was confirmed for these compositions, indicating that protons are the majority charge carriers.

Besides increasing the atomic ratio between the rare earth elements and Nb in the B-site, oxygen vacancies can also be introduced by acceptor-doping into the A-site, and divalent Ca, Sr and Ba are common dopants to partially substitute trivalent La. A comparison of the conductivities of the LNY system and those of some state-of-the-art proton conductors are summarized in Fig. 7. The conductivity of $La_2(Nb_{0.4}Y_{0.6})_2O_{7-\delta}$ (LNY60) is 3.17×10^{-4} S cm^{-1} at 700 °C in wet hydrogen (p_{H_2O} = 0.05 atm), and increases by nearly four times to 1.16×10^{-3} S cm^{-1} by doping 2.54 at% Ca (La + Ca = 100 at%).[96] Similarly, the conductivity of $La_2(Nb_{0.35}Y_{0.65})_2O_{7-\delta}$ (LNY65) increases from 2.88×10^{-4} S cm^{-1} to 1.16×10^{-3} S cm^{-1} by doping 0.98 at% Sr (La + Sr = 100 at%),[95] and the conductivity of LNYb55 increases from 2.78×10^{-4} S cm^{-1} to 4.51×10^{-4} S cm^{-1} by doping 3 at% Ca (La + Ca = 100 at%).[94] Anyhow, the conductivity of this system is still too low to be directly used as the electrolyte, but it may be potentially applicable as a buffer layer between the electrode and electrolyte of acceptor-doped $BaZrO_3$ and Ba(Zr, Ce)O_3, based on the superior chemical stability of LNY and LNYb55.

In addition, the generation of electron hole conduction in an oxidizing atmosphere is a problem for the acceptor-doped $BaZrO_3$ and Ba(Zr, Ce)O_3 electrolytes. For example, the state-of-the art $BaZr_{0.8}Y_{0.2}O_{3-\delta}$ electrolyte has the transport number of ionic conduction (t_{ion}) of 0.79 and 0.43 in wet oxygen (p_{H_2O} = 0.05 atm) at 600 and 700 °C, respectively. Remarkably, LNY and LNYb55 have higher t_{ion}, which is 0.92 and 0.80 at 600 and 700 °C, respectively, for LNY65,[96] and 0.95 and 0.90 at 600 and 700 °C, respectively, for $(La_{0.99}Ca_{0.01})_2(Nb_{0.45}Yb_{0.55})_2O_{7-\delta}$.[95] Therefore, depositing the LNY/LNYb55 electrolyte onto the Ba-based perovskite electrolytes will be a feasible strategy to improve the chemical stability and transport properties of the electrolyte.

The long-range and local crystal structures were also analyzed. Based on Rietveld refinement of powder XRD patterns of pristine and alkaline earth element-doped LNYb55, it was found that the 8b O2 site – in the center of the tetrahedrons containing four La cations – was fully occupied by oxide ions.

© 2024 The Author(s). Published by the Royal Society of Chemistry

Open Access Article. Published on 08 September 2023. Downloaded on 6/11/2026 10:35:40 PM. This article is licensed under a Creative Commons Attribution 3.0 Unported Licence.

The oxygen vacancies which were introduced by elevating the atomic ratio between Yb and Nb over unity and partially substituting trivalent La with divalent Ca, Sr and Ba cations located solely in the 48f O1 site, which is in the center of the tetrahedrons composed of two La and two Nb/Yb cations.[95] Furthermore, the results of extended X-ray absorption fine structure (EXAFS) analysis indicated that the coordination number of oxide ions in the vicinity of Y in the hydrated $La_2(Nb_{1-x}Y_x)_2O_{7-\delta}$ (x = 0.60, 0.65) samples is higher than those of the dried samples,[96] indicating that only the oxide ions/oxygen vacancies close to Y are active for the hydration reaction, and the oxygen vacancies formed by acceptor-doping prefer to be located in the vicinity of Y than Nb. Thereby, it is reasonable to conclude that even in the tetrahedrons composed of two La and two Nb/Yb or Y cations, oxygen vacancies prefer to form in the tetrahedrons containing La and Y or Yb, rather than those with Nb, suggesting a potential strategy to further improve the hydration ability and proton conduction by regulating the coordination of the local tetrahedrons in this class of materials.

3.3 Other materials

3.3.1 Zirconates. Shlyakhtina *et al.* prepared $(Gd_{0.975}Ca_{0.025})_2Zr_2O_{7-\delta}$ with a mechanical activation method, and the sample was finally heated at 1600 °C.[100] After measuring the impedance spectra in both dry and wet air, they found that the total conductivity of $(Gd_{0.975}Ca_{0.025})_2Zr_2O_{7-\delta}$ changed little in the two different atmospheres, indicating that the proton conduction is negligible in this material. It is noteworthy the crystal structure of $(Gd_{0.975}Ca_{0.025})_2Zr_2O_{7-\delta}$ is not clear, but it shows the feature matching the fluorite structure model. The authors also prepared $Sm_2Zr_2O_7$ and $(Sm_{0.975}Ca_{0.025})_2Zr_2O_{7-\delta}$ pyrochlore oxides. Although $Sm_2Zr_2O_7$ shows no proton conduction, by doping Ca into the Sm-site, the sample shows lower conduction activation energy in wet air at the temperature below 600 °C, compared with that in dry air. Moreover, both the bulk and grain boundary conductivities were higher in wet air, indicating the generation of proton conduction. At 530 °C in wet air (p_{H_2O} = 0.023 atm), the proton conductivity of $(Sm_{0.975}Ca_{0.025})_2Zr_2O_{7-\delta}$ is 2.4×10^{-5} S cm^{-1}.[100] The authors further prepared $Nd_2Zr_2O_7$ and $(Nd_{0.975}Ca_{0.025})_2Zr_2O_{7-\delta}$ pyrochlore oxides. The conductivity of these oxides was also higher in wet air, indicating the presence of proton conductivity. At 500 °C, the proton conductivity of $Nd_2Zr_2O_7$ was approximately 5.0×10^{-6} S cm^{-1}, and increased to 1.0×10^{-5} S cm^{-1} at 600 °C. The proton conductivity of $(Nd_{0.975}Ca_{0.025})_2Zr_2O_{7-\delta}$ was approximately 7.0×10^{-5} and 2.5×10^{-4} S cm^{-1} at 500 and 600 °C, respectively.[101] As has been mentioned, by using La to occupy the A-site, the resulting $La_2Zr_2O_7$ system also exhibits proton conduction, and the highest proton conductivity was reported for $(La_{0.975}Ca_{0.025})_2Zr_2O_{7-\delta}$ to be 6.8×10^{-4} S cm^{-1} at 600 °C.[81] Interestingly, one may notice that the proton conductivity increases in the sequence of $Gd_2Zr_2O_7 < Sm_2Zr_2O_7 < Nd_2Zr_2O_7 < La_2Zr_2O_7$, in agreement with the increasing eight-coordinated cation radius of Gd^{3+} (1.053 Å) < Sm^{3+} (1.079 Å) < Nd^{3+} (1.109 Å) < La^{3+} (1.160 Å).[11] These results indicate that the size of the A-site cation has a significant effect on the proton conduction of pyrochlore zirconates.

3.3.2 Stannates. The proton conductivity of pyrochlore stannates also exhibits a dependence on the cation radius at the A-site. Eurenius *et al.* prepared Ca-doped $A_2Sn_2O_7$ (A = La, Sm, Yb) using the solid-state reaction method, and studied the conduction behavior in dry and wet atmospheres.[102] The results showed that the conductivity of $(A_{0.98}Ca_{0.02})_2Sn_2O_{7-\delta}$ (Ln = La, Sm, Yb) at the temperature lower than 500 °C in wet Ar (p_{H_2O} = 0.026 atm) was higher than that in dry Ar. Additionally, a clear H_2O/D_2O isotope effect was observed, indicating the presence of proton conduction. The conductivities in wet Ar were subtracted by those in wet Ar to estimate the proton conductivities, which were 5.8×10^{-9}, 2.3×10^{-7} and 3.0×10^{-7} S cm^{-1} 300 °C for $(Yb_{0.98}Ca_{0.02})_2Sn_2O_{7-\delta}$, $(La_{0.98}Ca_{0.02})_2Sn_2O_{7-\delta}$ and $(Sm_{0.98}Ca_{0.02})_2Sn_2O_{7-\delta}$, respectively. It is clear that by using larger La^{3+} (1.160 Å) and Sm (1.079 Å) to occupy the A-site of the pyrochlore stannates, higher proton conductivity can be obtained, compared with the case using smaller Yb^{3+} (0.98 Å). Eurenius *et al.* also prepared undoped $Sm_2Sn_2O_7$, $(Sm_{0.96}Ca_{0.04})_2Sn_2O_{7-\delta}$, and $Sm_2(Sn_{0.96}Y_{0.04})_2O_{7-\delta}$.[103] The proton conductivities at 300 °C in wet Ar (p_{H_2O} = 0.026 atm) were found to be 2.5×10^{-8} and 2.6×10^{-6} S cm^{-1} for $Sm_2Sn_2O_7$ and $(Sm_{0.96}Ca_{0.04})_2Sn_2O_{7-\delta}$, respectively. By comparing with the aforementioned results of $(Sm_{0.98}Ca_{0.02})_2Sn_2O_{7-\delta}$, one can see that the conductivity increases with the increasing Ca concentration, indicating that Ca is an effective dopant to enhance the proton conduction in $Sm_2Sn_2O_7$. $Sm_2(Sn_{0.96}Y_{0.04})_2O_{7-\delta}$ shows proton conductivity of 3.4×10^{-9} S cm^{-1} at 300 °C, even lower than that of undoped $Sm_2Sn_2O_7$.

3.3.3 Titanates. Although it has not been studied as deeply as pyrochlore zirconates, some titanates have also been investigated for proton conductors. Fjeld *et al.* prepared $Er_{1.96}Ca_{0.04}Ti_2O_{7-\delta}$ pyrochlore titanates using the citrate–nitrate method, but found no presence of proton conduction in this material.[104] Shimura *et al.* prepared $Y_2(Ti_{0.9}B_{0.1})_2O_{7-\delta}$ (B = In, Mg) pyrochlore phase oxide with the solid-state reaction method, but still observed no significant proton conduction.[77] Later, Eurenius *et al.* synthesized $(Sm_{0.96}Ca_{0.04})_2Ti_2O_{7-\delta}$ and $Sm_2(Ti_{0.96}Y_{0.04})_2O_{7-\delta}$, and confirmed a significant increase in bulk conductivity of these materials under wet conditions below 500 °C as compared to that under dry conditions, indicating the presence of proton conduction.[105] The proton conductivities of $(Sm_{0.96}Ca_{0.04})_2Ti_2O_{7-\delta}$ and $Sm_2(Ti_{0.96}Y_{0.04})_2O_{7-\delta}$ are 1.2×10^{-5} and 3.3×10^{-6} S cm^{-1}, respectively, at 300 °C in wet oxygen (p_{H_2O} = 0.026 atm). The authors further used an electromotive force (EMF) method on gas concentration cells, and determined that $(Sm_{0.96}Ca_{0.04})_2Ti_2O_{7-\delta}$ has $t_{H^+} > 0.9$ at 400 °C under a wet oxygen atmosphere. In summary, the pyrochlore titinates with small A-site cations (Y^{3+} (1.019 Å), Er^{3+} (1.004 Å)) do not exhibit proton conduction. When the A-site is occupied by larger cations like Sm^{3+} (1.079 Å), proton conduction is generated.[106]

3.4 Dependence of hydration ability on cation radius

One interesting conclusion from the 3.3 section is that in the system with the same B-site cation, the proton conductivity

Open Access Article. Published on 08 September 2023. Downloaded on 6/11/2026 10:35:40 PM.
This article is licensed under a Creative Commons Attribution 3.0 Unported Licence.

increases with the increasing size of the A-site cation. In addition, a relationship can also be found between the B-site cation and the proton conduction of the pyrochlore oxides. Eurenius *et al.* found that the conductivities of pre-hydrated $(Sm_{0.96}Ca_{0.04})_2B_2O_{7-\delta}$ (B = Ti, Zr, Sn) decreased when the samples were exposed to dry Ar due to the loss of protons resulting from dehydration.[107] By assuming the decrement in conductivity caused by dehydration to the proton conductivity, the proton conductivities of $(Sm_{0.96}Ca_{0.04})_2Ti_2O_{7-\delta}$, $(Sm_{0.96}Ca_{0.04})_2Sn_2O_{7-\delta}$ and $(Sm_{0.96}Ca_{0.04})_2Zr_2O_{7-\delta}$ at 300 °C can be estimated to be 3.12×10^{-5}, 1.68×10^{-6} and 9.39×10^{-8} S cm^{-1}, respectively, decreasing with the increasing radius of the B-site cation (Ti^{4+}(0.605 Å) < Sn^{4+}(0.690 Å) < Zr^{4+} (0.72 Å)[11]). Therefore, the proton conduction in pyrochlore oxides can be expected to be dependent on the size of cations in the A and B-sites, which were revealed to influence the hydration ability and thereby the proton concentration significantly.

Eurenius *et al.* measured the proton concentration of $(A_{0.98}Ca_{0.02})_2Sn_2O_{7-\delta}$ (A = La, Sm, Yb) after annealing at 300 °C in wet nitrogen (p_{H_2O} = 0.37 atm), which was 2.85×10^{-5}, 2.10×10^{-5} and 1.62×10^{-5} mol cm^{-3} for $(La_{0.98}Ca_{0.02})_2Sn_2O_{7-\delta}$, $(Sm_{0.98}Ca_{0.02})_2Sn_2O_{7-\delta}$ and $(Yb_{0.98}Ca_{0.02})_2Sn_2O_{7-\delta}$, respectively, and decreased with the decreasing size of the A-site cations (La^{3+} (1.160 Å) > Sm^{3+} (1.079 Å) > Yb^{3+} (0.985 Å)[11]).[102] This finding is consistent with the results of Bjørheim *et al.* that the proton concentration decreased in the sequence of $La_{1.8}Ca_{0.2}Sn_2O_{7-\delta}$ > $Sm_{1.8}Ca_{0.2}Sn_2O_{7-\delta}$ > $Er_{1.8}Ca_{0.2}Sn_2O_{7-\delta}$ with Er^{3+} (1.004 Å[11]) to be the smallest A-site cation in their study.[108] Since the protons are introduced through the hydration reaction (eqn (1)), the equilibrium constant can be given as

$$K_{hydr} = \exp\left(\frac{\Delta_{hydr}S^\circ}{R}\right)\exp\left(-\frac{\Delta_{hydr}H^\circ}{RT}\right) \quad (6)$$

where $\Delta_{hydr}S^\circ$ and $\Delta_{hydr}H^\circ$ are the changes in standard hydration entropy and hydration enthalpy, respectively, T is temperature, and R is the gas constant. $\Delta_{hydr}S^\circ$ seems to be affected little by the composition, typically falling within -120 ± 40 J mol^{-1} K^{-1}. $\Delta_{hydr}H^\circ$ depends on the properties of the material, and an exothermic hydration reaction has negative value of $\Delta_{hydr}H^\circ$.[72] Bjørheim *et al.* used first principles density functional theory (DFT) to calculate $\Delta_{hydr}H^\circ$ of $A_2B_2O_7$ (A = La–Lu, B = Ti, Sn, Zr, Ce).[108] As shown in Fig. 8, when the B-site cations are the same, the absolute value of $\Delta_{hydr}H^\circ$ increases with the increasing radius of the A-site cations.

$\Delta_{hydr}H^\circ$ also correlates with the radii of the B-site cations. As shown in Fig. 8, when the A-site is occupied by Lu, Er, Y and Sm, a larger absolute value of $\Delta_{hydr}H^\circ$ is obtained when the B-site is occupied by a small cation (*e.g.*, Ti^{4+}) compared with a large cation (*e.g.*, Sn^{4+}). However, when Gd and La occupy the A-site, the absolute value of $\Delta_{hydr}H^\circ$ is larger when the B-site is occupied by Zr^{4+}, which is larger than Sn^{4+}. Eurenius *et al.* also measured the proton concentration of $(Sm_{0.96}Ca_{0.04})_2B_2O_{7-\delta}$ (B = Ti, Sn, Zr) hydrated at 300 °C in wet nitrogen (p_{H_2O} = 0.37 atm), which were 4.76×10^{-4}, 4.97×10^{-4} and 8.69×10^{-5} mol cm^{-3} for $(Sm_{0.96}Ca_{0.04})_2Ti_2O_{7-\delta}$, $(Sm_{0.96}Ca_{0.04})_2Sn_2O_{7-\delta}$, and $Sm_{1.92}Ca_{0.08}Zr_2O_{7-\delta}$, respectively.[107] These results

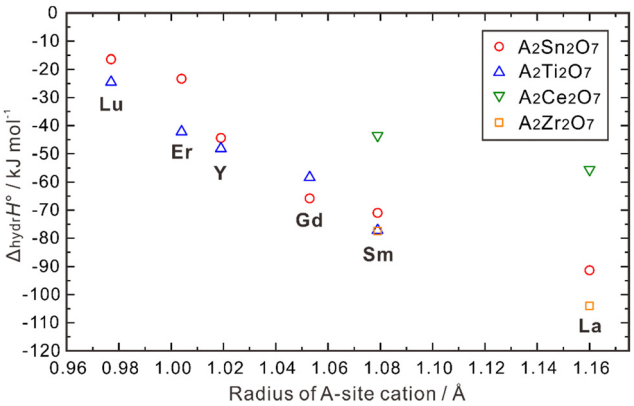

Fig. 8 Calculated hydration enthalpies for pyrochlore structured $A_2B_2O_7$ (B = Ti, Sn, Zr, Ce).[108]

indicate that although there are some exceptions, small cations in the B-site in general favors the hydration reaction in the pyrochlore oxides. The ordering and stability of the pyrochlore structure seem to correlate with the ratio of cation radii ($r_{A^{3+}}/r_{B^{4+}}$). As this ratio increases, the stability and ordering of the pyrochlore increase.[12] Consequently, when the size of A^{3+} ions increase and that of B^{4+} ions decrease, the degree of ordering in the pyrochlore structure is likely to increase, potentially leading to a more negative hydration enthalpy, which in turn benefits proton incorporation.

4. Applications

4.1 Intermediate temperature fuel cells

$La_2Ce_2O_7$-based materials have already been used as electrolytes in fuel cells,[109–113] which were demonstrated as protonic ceramic fuel cells (PCFCs, Fig. 9(a)) where the main charge carriers in the electrolyte are protons. However, since the $La_2Ce_2O_7$-based materials exhibit mixing ionic conduction of protons and oxides in the intermediate temperature range (450–700 °C), and oxide ions are in fact the majority charge carriers at relatively high temperature (*e.g.*, 700 °C), it is not appropriate to claim them as PCFCs. Anyway, we summarize the performance of the reported fuel cells using the $La_2Ce_2O_7$-based electrolytes in Table 1 for information, from which one can see that compared with pure $La_2Ce_2O_7$, the fuel cells using the doped $La_2Ce_2O_7$ electrolyte show higher performance. Besides, by regulating the compositions of the electrolyte, the performance of the fuel cells can be optimized. For example, as shown in Fig. 10, the fuel cell using a $(La_{0.925}Mg_{0.075})_2Ce_2O_{7-\delta}$ electrolyte exhibits the highest P_{max} of 897 mW cm^{-2} at 700 °C, due to the highest ionic conductivity of the electrolyte among the compositions studied.[110] This fuel cell also shows P_{max} of 223 mW cm^{-2} at 550 °C, which is consistent with the trend of conductivity.[110] Similarly, the fuel cell utilizing a $(Nd_{0.925}Mg_{0.075})_2Ce_2O_{7-\delta}$ electrolyte demonstrates P_{max} of 483 mW cm^{-2} and an open circuit voltage (OCV) of 0.890 V at 700 °C, which are the highest value for the fuel cells using the (Nd, Mg)$_2Ce_2O_{7-\delta}$-based electrolytes.[113] It deserves noting that these

© 2024 The Author(s). Published by the Royal Society of Chemistry

Open Access Article. Published on 08 September 2023. Downloaded on 6/11/2026 10:35:40 PM.
This article is licensed under a Creative Commons Attribution 3.0 Unported Licence.

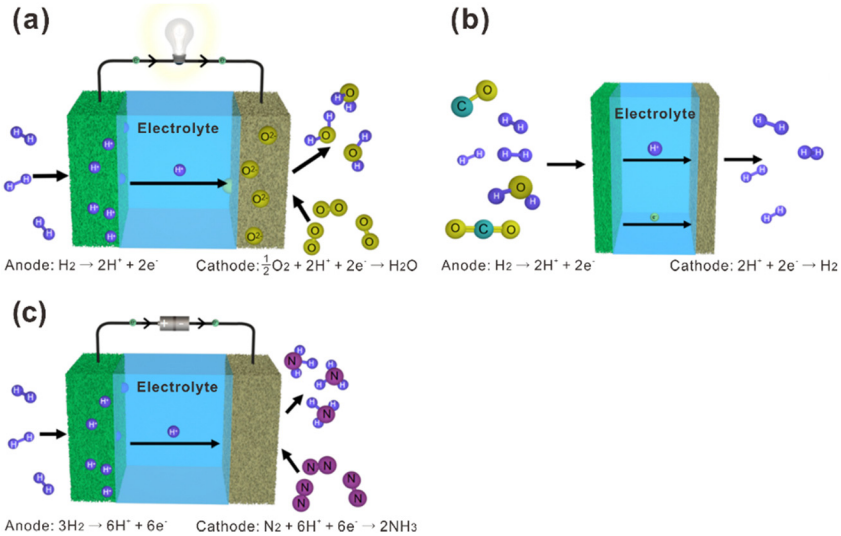

Fig. 9 Schematic diagrams of (a) fuel cells, (b) hydrogen separation membranes, and (c) ammonia synthesis based on proton-conducting electrolytes.

fluorite-based oxides exhibit excellent chemical stability in CO_2 and H_2O atmospheres, and a much longer lifetime is thereby expected compared with the case using some Ba-based perovskite electrolytes.[9]

4.2 Hydrogen separation membrane

Proton and electron mixed conducting ceramic membranes are an ideal solution for separating H_2 due to its excellent stability, high hydrogen selectivity and low cost.[118] As shown in Fig. 9(b), H_2 molecules are firstly adsorbed on the surface of the membrane and dissociated into protons and electrons. Then, protons move across the electrolyte to the other side of the membrane, where they recombine with electrons to form H_2 molecules. The current technologies for ceramic separation membranes can be classified into two types. One is metal-ceramic composite membranes, where the metal and ceramic phases conduct electrons and protons, respectively. The other is single-phase ceramics, which are mixed conductors of protons and electrons. Some state-of-the art proton conductors – such as $SrCeO_3$ and $BaCeO_3$ – have been doped with multivalent dopants to make them conduct electrons simultaneously. However, $BaCeO_3$ and $SrCeO_3$ are chemically unstable and easily react with CO_2 and H_2O.[119,120] On the other hand, fluorite-based oxide membranes exhibit excellent stability in H_2O and CO_2, making them a promising option for hydrogen separation, and the progresses are summarized in Table 2. Fig. 11 shows the hydrogen permeation flux across the membrane of $La_2Ce_2O_7$ doped with various concentrations of Sm, and $(La_{0.975}Sm_{0.025})_2Ce_2O_{7-\delta}$ is the optimical composition, showing the highest hydrogen permeation flux.[121] Besides, the hydrogen permeation flux is influenced not only by the conduction properties (*e.g.*, electron conductivity and proton conductivity) of the material, but also by temperature, hydrogen gradient, and film thickness.

Table 1 Reported performance of fuel cells using $La_2Ce_2O_7$-based electrolytes with wet hydrogen used as the fuel

Electrolyte	Anode	Cathode	Electrolyte thickness/ μm	Operating temperature/ °C	P_{max}/ mW cm^{-2}	OCV/ V	Ref.
$La_2Ce_2O_7$	Ni-$BaZr_{0.1}Ce_{0.7}Y_{0.2}O_{3-\delta}$	$La_{0.6}Sr_{0.4}Co_{0.2}Fe_{0.8}O_{3-\delta}$–$Sm_{0.2}Ce_{0.8}O_{2-\delta}$	40	550	80	1.07	109
$(La_{0.925}Mg_{0.075})_2Ce_2O_{7-\delta}$	Ni-$La_{1.85}Mg_{0.15}Ce_2O_{7-\delta}$	$Sm_{0.5}Sr_{0.5}CoO_{3-\delta}$–$Ce_{0.8}Sm_{0.2}O_{2-\delta}$	15	550	223	0.95	110
$(La_{0.925}Na_{0.075})_2Ce_2O_{7-\delta}$	Ni-$La_{1.85}Na_{0.15}Ce_2O_{7-\delta}$	$Ba_{0.5}Sr_{0.5}Co_{0.8}Fe_{0.2}O_{3-\delta}$–$La_{1.85}Na_{0.15}Ce_2O_{7-\delta}$	53	600	154	0.95	111
$(La_{0.975}Ca_{0.025})_2Ce_2O_{7-\delta}$	Ni-$La_{1.95}Ca_{0.05}Ce_2O_{7-\delta}$	$LaSr_3Co_{1.5}Fe_{1.5}O_{10-\delta}$–$La_{1.95}Ca_{0.05}Ce_2O_{7-\delta}$	15	600	149	0.86	114
$(La_{0.925}Mo_{0.075})_2Ce_2O_{7-\delta}$	Ni-$La_{1.85}Mo_{0.15}Ce_2O_{7-\delta}$	$Ba_{0.5}Sr_{0.5}Co_{0.8}Fe_{0.2}O_{3-\delta}$–$La_{1.85}Mo_{0.15}Ce_2O_{7-\delta}$	52	600	290	0.90	115
$(La_{0.95}In_{0.05})_2Ce_2O_{7-\delta}$	Ni-$BaCe_{0.5}Zr_{0.3}Dy_{0.2}O_{3-\delta}$	$Ba_{0.5}Sr_{0.5}Co_{0.8}Fe_{0.2}O_{3-\delta}$–$La_{1.90}In_{0.10}Ce_2O_{7-\delta}$	46	550	179	0.94	116
$(La_{0.95}In_{0.05})_2Ce_2O_{7-\delta}$	Ni-$La_{1.90}In_{0.10}Ce_2O_{7-\delta}$	$Ba_{0.5}Sr_{0.5}Co_{0.8}Fe_{0.2}O_{3-\delta}$–$La_{1.90}In_{0.10}Ce_2O_{7-\delta}$	40	550	121	1.09	116
$(La_{0.925}Rb_{0.075})_2Ce_2O_{7-\delta}$	Ni-$La_{1.85}Rb_{0.15}Ce_2O_{7-\delta}$	$Sm_{0.5}Sr_{0.5}Co_3$–$Ce_{0.8}Sm_{0.2}O_{2-\delta}$	15	700	1065	0.88	117
$(Nd_{0.925}In_{0.075})_2Ce_2O_{7-\delta}$	Ni–$Nd_{1.85}In_{0.15}Ce_2O_{7-\delta}$	$Ba_{0.5}Sr_{0.5}Co_{0.8}Fe_{0.2}O_{3-\delta}$–$Nd_{1.85}In_{0.15}Ce_2O_{7-\delta}$	46	550	165	0.93	112
$Nd_2Ce_2O_7$	Ni–$Nd_2Ce_2O_7$	$Ba_{0.5}Sr_{0.5}Co_{0.8}Fe_{0.2}O_{3-\delta}$–$Nd_2Ce_2O_7$	50	700	397	0.859	113
$Nd_{1.85}Mg_{0.15}Ce_2O_{7-\delta}$	Ni–$Nd_2Ce_2O_7$	$Ba_{0.5}Sr_{0.5}Co_{0.8}Fe_{0.2}O_{3-\delta}$–$Nd_2Ce_2O_7$	50	700	483	0.890	113
$Nd_{1.85}Ca_{0.15}Ce_2O_{7-\delta}$	Ni–$Nd_2Ce_2O_7$	$Ba_{0.5}Sr_{0.5}Co_{0.8}Fe_{0.2}O_{3-\delta}$–$Nd_2Ce_2O_7$	50	700	428	0.864	113
$Nd_{1.85}Sr_{0.15}Ce_2O_{7-\delta}$	Ni–$Nd_2Ce_2O_7$	$Ba_{0.5}Sr_{0.5}Co_{0.8}Fe_{0.2}O_{3-\delta}$–$Nd_2Ce_2O_7$	50	700	441	0.873	113
$Nd_{1.85}Ba_{0.15}Ce_2O_{7-\delta}$	Ni–$Nd_2Ce_2O_7$	$Ba_{0.5}Sr_{0.5}Co_{0.8}Fe_{0.2}O_{3-\delta}$–$Nd_2Ce_2O_7$	50	700	418	0.878	113

Open Access Article. Published on 08 September 2023. Downloaded on 6/11/2026 10:35:40 PM.
This article is licensed under a Creative Commons Attribution 3.0 Unported Licence.

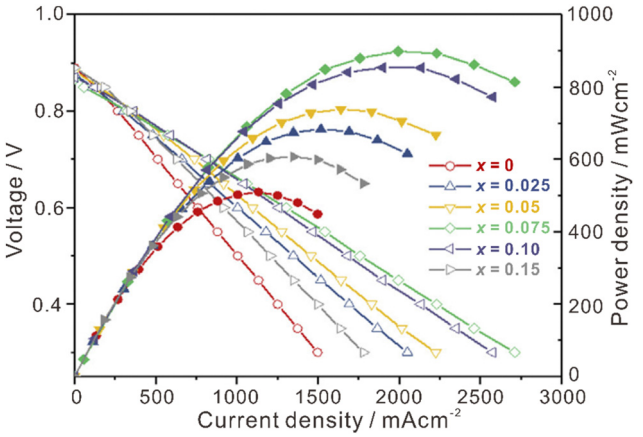

Fig. 10 Performance of fuel cells at 700 °C using $(La_{1-x}Mg_x)_2Ce_2O_{7-\delta}$ as the electrolyte. Reprinted with permission,[110] Copyright [2019] Elsevier.

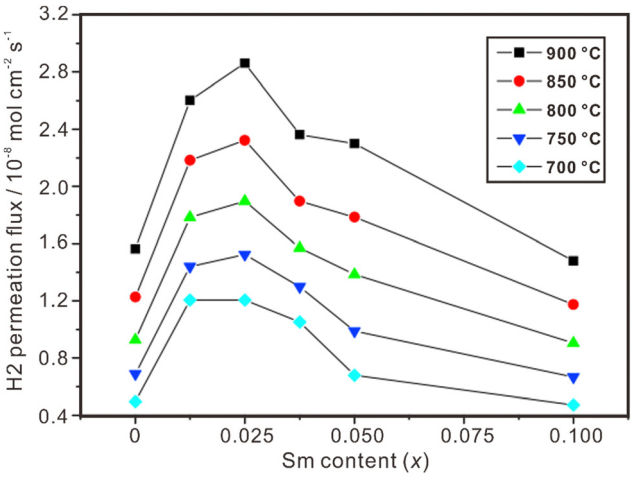

Fig. 11 Hydrogen permeation flux through Ni-$(La_{1-x}Sm_x)_2Ce_2O_{7-\delta}$ membranes. Reprinted with permission,[121] Copyright [2010] Elsevier.

The hydrogen permeation flux increases with the increasing temperature, decreasing film thickness and increasing hydrogen gradient.

Generally, for H_2 separation at an industrial level, the ceramic membrane must have partial conductivities of protons and electrons both higher than 0.1 S cm^{-1}, leading to the hydrogen permeation flux exceeding 3.7×10^{-5} mol cm^{-2} s^{-1}.[122] Unfortunately, at present, the conductivity of the fluorite-based oxide membranes is still too low to satisfy the requirements. Nonetheless, this technology is still considered to be a promising alternative for H_2 separation due to the excellent H_2 selectivity, high energy efficiency, low cost and excellent long-term stability, demanding continuous effort for development in the future.

4.3 Ammonia synthesis

Ammonia (NH_3) is an important raw material for the chemical industry and a convenient medium for energy storage.[128,129] The Haber–Bosch method is a conventional approach toward NH_3 synthesis, involving the reaction of gaseous hydrogen and nitrogen on a catalyst at high temperature (450–500 °C) and high pressure (15–30 MPa),[130,131] following

$$N_2 + 3H_2 = 2NH_3 \quad (7)$$

Due to the high temperature and high pressure required for the reaction, specialized equipment is necessary, and the conversion efficiency is low (10–15%)[131] and energy consumption is high. A new method has thereby been proposed by using proton-conducting ceramics to electrochemically synthesize NH_3, as shown in Fig. 9(c). Here, H_2 molecules are dissociated into protons and electrons at the anode:

$$3H_2 \rightarrow 6H^+ + 6e^- \quad (8)$$

Protons move across the proton-conducting ceramic to the cathode, where they react with N_2 and electrons to form NH_3:

$$N_2 + 6H^+ + 6e^- \rightarrow 2NH_3 \quad (9)$$

Electrochemical synthesis is a promising method overcoming thermodynamic limitations of conventional catalytic reactors and significantly improving the conversion efficiency (around 80%).[129,130] It can be carried out under normal pressure, which reduces equipment requirements and costs. Due to these advantages, efforts have been dedicated continuously to the development of the electrochemical synthesis of NH_3 using proton-conducting ceramics (Table 3), and the NH_3 production

Table 2 Reported performance of hydrogen separation membranes using fluorite-based oxides

Material	Feed gas/sweep gas	Film thickness/μm	Operating temperature/°C	Hydrogen permeation flux/mol cm^{-2} s^{-1}	Ref.
$Ni\text{-}La_2Ce_2O_7$	wet 20% H_2 in N_2 (3% H_2O)/Ar	600	900	1.6×10^{-8}	123
$Ni\text{-}(La_{0.975}Ca_{0.025})_2Ce_2O_{7-\delta}$	wet 20% H_2 in N_2 (3% H_2O)/Ar	600	900	1.9×10^{-8}	123
$Ni\text{-}(La_{0.95}Ca_{0.05})_2Ce_2O_{7-\delta}$	wet 20% H_2 in N_2 (3% H_2O)/Ar	600	900	1.4×10^{-8}	123
$Ni\text{-}La_2Ce_2O_7$	wet 20% H_2 in N_2 (3% H_2O)/Ar	48	900	6.83×10^{-8}	124
$La_2Ce_2O_7$	wet 20% H_2 in N_2 (3% H_2O)/Ar	30	900	2.6×10^{-8}	125
$Ni\text{-}Ce_{0.8}Sm_{0.2}O_{2-\delta}$	40% H_2 in N_2/Ar	35	900	1.5×10^{-9}	126
$Ni\text{-}Ce_{0.8}Sm_{0.2}O_{2-\delta}$	40% H_2 in N_2/Ar	21	900	3.0×10^{-9}	126
$Ni\text{-}(La_{0.975}Sm_{0.025})_2Ce_2O_{7-\delta}$	wet 20% H_2 in N_2 (3% H_2O)/Ar	600	900	2.86×10^{-8}	121
$Ni\text{-}(La_{0.975}Sm_{0.025})_2Ce_2O_{7-\delta}$	wet 20% H_2 in N_2 (3% H_2O)/Ar	600	900	2.30×10^{-8}	121
CeO_2	wet 7.9% H_2 in N_2 (2.5% H_2O)/Ar	3930	777	9.44×10^{-11}	65
$Ce_{0.9}Ca_{0.1}O_{2-\delta}$	wet 7.6% H_2 in N_2 (2.2% H_2O)/Ar	3800	800	6.67×10^{-11}	127
$Ce_{0.85}Ca_{0.15}O_{2-\delta}$	wet 7.6% H_2 in N_2 (2.3% H_2O)/Ar	3500	777	9.76×10^{-12}	68
$Ce_{0.9}Gd_{0.1}O_{2-\delta}$	wet 7.2% H_2 in N_2 (2.3% H_2O)/Ar	3500	780	8.06×10^{-12}	66
$Ce_{0.8}Yb_{0.2}O_{2-\delta}$	wet 7.9% H_2 in N_2 (2.6% H_2O)/Ar	3920	777	9.26×10^{-12}	67

© 2024 The Author(s). Published by the Royal Society of Chemistry

Table 3 Reported performance of electrochemical ammonia synthesis using fluorite-based oxides

Material	Flow rate at cathode (dry N_2)/m^3 s^{-1}	Flow rate at anode (wet H_2)/m^3 s^{-1}	Voltage/V	Operating temperature/°C	NH_3 production rate/ mol cm^{-2} s^{-1}	Ref.
$La_{1.9}Ca_{0.1}Zr_2O_{7-\delta}$	3.0×10^{-4}	1.0×10^{-4}	0.6	520	1.756×10^{-9}	138
$La_{1.95}Ca_{0.05}Zr_2O_{7-\delta}$	3.0×10^{-10}	1.0×10^{-10}	0.6	520	1.965×10^{-9}	139
$La_{1.95}Ca_{0.05}Ce_2O_{7-\delta}$	3.0×10^{-10}	1.0×10^{-10}	0.6	520	1.300×10^{-9}	139
$Ce_{0.8}La_{0.2}O_{2-\delta}$	3.0×10^{-4}	1.0×10^{-4}	0.6	650	7.061×10^{-9}	140
$Ce_{0.8}Y_{0.2}O_{2-\delta}$	3.0×10^{-4}	1.0×10^{-4}	0.6	650	7.319×10^{-9}	140
$Ce_{0.8}Gd_{0.2}O_{2-\delta}$	3.0×10^{-4}	1.0×10^{-4}	0.6	650	7.552×10^{-9}	140
$Ce_{0.8}Sm_{0.2}O_{2-\delta}$	3.0×10^{-4}	1.0×10^{-4}	0.6	650	7.955×10^{-9}	140

Open Access Article. Published on 08 September 2023. Downloaded on 6/11/2026 10:35:40 PM. This article is licensed under a Creative Commons Attribution 3.0 Unported Licence.

rate has been increased to 10^{-10}–10^{-8} mol cm^{-2} s^{-1}.[128] The device consists of a dense electrolyte and two porous electrodes (anode and cathode). The electrolyte facilitates proton transport and functions as a barrier for gas diffusion, effectively separating the gases from the two electrodes. By combining the proton conductor with the cathode and electrochemically supplying protons to the catalyst, the synthesis rate of ammonia can be enhanced. The fluorite-based proton conductors demonstrate proton conductivity in hydrogen-containing atmospheres with excellent chemical stability in both oxidizing and reducing environments. Consequently, electrochemical processes that utilize fluorite-based proton conductors as electrolytes offer alternatives for ammonia synthesis. However, this production rate is still far lower than the demands of practical application, requiring great breakthrough in the future.

The electrochemical synthesis of NH_3 is influenced significantly by the operating environment, including current density, temperature, materials for electrodes, electrolytes and catalysts. These factors greatly affect the production rate, selectivity, and energy utilization of NH_3. While it is true that increasing the current density can enhance the ammonia production rate, it does not always lead to a consistent increase, since high current density promotes the side reaction of hydrogen evolution at the cathode following eqn (10), which reduces the selectivity of ammonia.[132]

$$2H^+ + 2e^- \rightarrow H_2 \quad (10)$$

Due to the slow kinetics of nitrogen reduction, the production rate is low at room temperature, and can be accelerated at elevated temperature (*e.g.*, 500 °C). However, high temperature promotes the decomposition of ammonia and reduces the selectivity of ammonia.[133] The electronic conductivity of the electrode materials plays a crucial role in improving the rate of ammonia generation. Additionally, the polarization of the electrodes significantly impacts the rate of ammonia generation.[134] The electrolytes should have high proton conductivity and negligible electron conductivity and should be dense enough to maintain airtightness. The catalysts are essential for the electrochemical synthesis of NH_3 as they need to exhibit high selectivity towards ammonia while suppressing the hydrogen evolution reaction.

The electrochemical synthesis of ammonia faces several challenges, particularly in the development of materials that are highly active, selective and durable. In order to improve the selectivity of ammonia, it is vital to design the cathode which can effectively suppress the hydrogen evolution reaction. A key factor to increase the ammonia yield is to regulate and optimize the chemical adsorption of nitrogen on the cathode and the binding energy between nitrogen and catalyst. It is important to find a balanced binding energy, as weaker binding energy makes it difficult to reduce nitrogen and decreases ammonia yield, while a stronger binding energy leads to higher desorption energy and potential catalyst poisoning. It is reported that increasing the concentration of oxygen vacancies on the electrode surface can enhance the catalytic activity of nitrogen reduction and also inhibit the hydrogen evolution reaction.[135] Therefore, materials with a high concentration of oxygen vacancies can potentially be appropriate cathode candidates. Besides, the production rate and selectivity of ammonia can be influenced by current density and temperature, so it is also important to determine the optimal operating conditions to achieve a high production rate and selectivity. In addition, the proton conductivity of the electrolyte plays a crucial role in facilitating the transport of protons to the cathode for nitrogen reduction. Therefore, it is imperative to enhance the proton conductivity of the electrolyte in order to minimize ohmic loss. The electrolytes should also exhibit good chemical stability, mechanical strength, and negligible electronic conductivity. Additionally, reducing the thickness of the electrolyte further help in reducing ohmic loss.[136] Since the hydrogen evolution reaction is unavoidable, unreacted H_2 can be recycled back to the cathode to increase the utilization of hydrogen.[137] Moreover, in order to consistently achieve the electrochemical synthesis of NH_3 with optimal efficiency, the reactor should possess flexibility and be capable of operating across a wide range of conditions.

5. Conclusion remarks

In this work, we reviewed the material systems with a fluorite or pyrochlore crystal structure which show the volume conduction of protons, and described their potential applications in intermediate fuel cells, hydrogen separation membranes, and ammonia synthesis. However, it should be admitted that the fluorite structure-based proton conductors are presently not as successful as those with the perovskite structure for their application in the solid-state electrochemical devices, restricted by their low proton conductivity. To improve the proton conduction, increasing the concentration of oxygen vacancies is a common strategy taken in the system of perovskite oxides, but it does not work well in the fluorite-based oxides. For example, the proton conductivity of $Zr_{0.82}Y_{0.18}O_{2-\delta}$ (δ = 0.09) is only

Open Access Article. Published on 08 September 2023. Downloaded on 6/11/2026 10:35:40 PM. This article is licensed under a Creative Commons Attribution 3.0 Unported Licence.

1.5×10^{-8} S cm^{-1} at 777 °C,[46] and that of $Ce_{0.8}Yb_{0.2}O_{2-\delta}$ (δ = 0.1) is 1.0×10^{-6} S cm^{-1} at 727 °C.[67] In comparison, $BaZr_{0.8}Y_{0.2}O_{3-\delta}$ (δ = 0.1) with a similar concentration of oxygen vacancies (δ) has a proton conductivity of 2.45×10^{-2} S cm^{-1} at 700 °C,[141] more than four orders of magnitude higher than that of the doped ZrO_2 and CeO_2. Therefore, simply increasing the concentration of oxygen vacancies appears to have little chance to increase the proton conductivity of the fluorite oxides significantly. Based on the model suggested by Kalland *et al.*, the coordination environment directly impacts the ability of the oxide ions and oxygen vacancies to participate in the hydration reaction.[73] The oxide ions and oxygen vacancies surrounded by four relatively low valent cations (La^{3+} in the case of $La_2Ce_2O_7$) are active for the hydration reaction, but those surrounded by the cations with high oxidation state (Ce^{4+} in the case of $La_2Ce_2O_7$) appear to be resistive to the hydration reaction. A similar conclusion was also drawn by an EXAFS study on the local structure of $La_2(Nb_{1-x}Y_x)_2O_{7-\delta}$. The coordination number of oxide ions surrounding Y^{3+} and La^{3+} increased after hydration, but negligibly small change occurred in that surrounding the Nb^{5+} cations. Therefore, adjusting the coordination environment surrounding the oxide ions and oxygen vacancies is likely to be a more effective strategy, which can potentially improve the hydration ability and proton conduction of the oxides with the fluorite-based crystal structure.

Although the proton conductivity is still low, the chemical stability of the proton conducting fluorite structure-based oxides is excellent. Different from the state-of-the-art perovskite oxides with high proton conductivity (*e.g.*, Y-doped Ba(Zr, Ce)O_3), the proton conducting fluorite/pyrochlore oxides contain no main components of alkaline earth elements (*e.g.*, Ba). Even Ca, Sr and Ba are doped to improve the proton conduction, their solubility is very low (<3 at% (cation ratio)). Although at the present stage, it is difficult to directly apply the proton conducting fluorite/pyrochlore oxides as the electrolyte in protonic ceramic cells (PCCs), they can be used as a buffer layer – for example, between the Y-doped Ba(Zr, Ce)O_3 electrolyte and the electrodes – to avoid the direct contact of the electrolyte with the atmosphere containing water vapor and/or carbon dioxide. Besides, some pyrochlore oxides (*e.g.*, $La_2(Nb_{1-x}B_x)_2O_{7-\delta}$ (B = Y, Yb)) have a higher transport number than Y-doped Ba(Zr, Ce)O_3 in wet oxygen, so by inserting such a buffer layer between the Y-doped Ba(Zr, Ce)O_3 electrolyte and the oxygen electrode, the transport number of ionic conduction can be improved, leading to decreased leakage current and improved cell efficiency. However, the conventional co-sintering process results in interdiffusion between the buffer layer and electrolyte layer, and some other techniques which are free of high temperature heat-treatment (*e.g.*, pulsed layer deposition) are high in cost and not suitable for depositing large-area thin films. Therefore, breakthrough on the techniques to deposit high quality large-area thin films without high temperature heat-treatment is important towards the practical application of proton conducting ceramics in solid-state electrochemical devices.

Author contributions

Pan Xiang: formal analysis; writing – original draft; writing – review & editing. Sara Adeeba Ismail: formal analysis; writing – original draft. Shihang Guo: writing – original draft. Lulu Jiang: writing – original draft. Donglin Han: conceptualization; formal analysis; supervision; funding acquisition; writing – original draft; writing – review & editing.

Conflicts of interest

The authors declare no conflict of interest.

Acknowledgements

This work was supported by the Natural Science Foundation of Jiangsu Province (Grant No. BK20211071), the Natural Science Research Project of Jiangsu Higher Education Institutions (Grant No. 23KJA150009), the Key Technology Initiative of Suzhou Municipal Science and Technology Bureau (Grant No. SYG202011), the Project of Innovation and Entrepreneurship of Jiangsu Province (Grant No. JSSCRC2021526), and Soochow Municipal Laboratory for Low Carbon Technologies and Industries.

References

1 C. C. Duan, J. H. Tong, M. Shang, S. Nikodemski, M. Sanders, S. Ricote, A. Almansoori and R. O'Hayre, *Science*, 2015, **349**, 1321–1326.
2 C. C. Duan, R. Kee, H. Y. Zhu, N. Sullivan, L. Z. Zhu, L. Z. Bian, D. Jennings and R. O'Hayre, *Nat. Energy*, 2019, **4**, 230–240.
3 N. Taniguchi, T. Kuroha, C. Nishimura and K. Iijima, *Solid State Ionics*, 2005, **176**, 2979–2983.
4 S. Robinson, A. Manerbino and W. G. Coors, *J. Membr. Sci.*, 2013, **446**, 99–105.
5 S. Escolastico, C. Solis, C. Kjolseth and J. M. Serra, *Energy Environ. Sci.*, 2014, **7**, 3736–3746.
6 D. Clark, H. Malerod-Fjeld, M. Budd, I. Yuste-Tirados, D. Beeaff, S. Aamodt, K. Nguyen, L. Ansaloni, T. Peters, P. K. Vestre, D. K. Pappas, M. I. Valls, S. Remiro-Buenamanana, T. Norby, T. S. Bjorheim, J. M. Serra and C. Kjolseth, *Science*, 2022, **376**, 390–393.
7 C. Duan, R. J. Kee, H. Zhu, C. Karakaya, Y. Chen, S. Ricote, A. Jarry, E. J. Crumlin, D. Hook, R. Braun, N. P. Sullivan and R. O'Hayre, *Nature*, 2018, **557**, 217–222.
8 C. Zuo, S. Zha, M. Liu, M. Hatano and M. Uchiyama, *Adv. Mater.*, 2006, **18**, 3318–3320.
9 N. Zakowsky, S. Williamson and J. T. S. Irvine, *Solid State Ionics*, 2005, **176**, 3019–3026.
10 L. Minervini, R. W. Grimes and K. E. Sickafus, *J. Am. Ceram. Soc.*, 2000, **83**, 1873–1878.
11 R. D. Shannon, *Acta Crystallogr., Sect. A: Found. Crystallogr.*, 1976, **32**, 751–767.
12 M. A. Subramanian, G. Aravamudan and G. V. S. Rao, *Prog. Solid State Chem.*, 1983, **15**, 55–143.

© 2024 The Author(s). Published by the Royal Society of Chemistry

Open Access Article. Published on 08 September 2023. Downloaded on 6/11/2026 10:35:40 PM. This article is licensed under a Creative Commons Attribution 3.0 Unported Licence.

13 P. E. Blanchard, R. Clements, B. J. Kennedy, C. D. Ling, E. Reynolds, M. Avdeev, A. P. Stampfl, Z. Zhang and L. Y. Jang, *Inorg. Chem.*, 2012, **51**, 13237–13244.
14 H. Yamamura, H. Nishino, K. Kakinuma and K. Nomura, *Solid State Ionics*, 2003, **158**, 359–365.
15 T. Moriga, A. Yoshiasa, F. Kanamaru, K. Koto, M. Yoshimura and S. Somiya, *Solid State Ionics*, 1989, **31**, 319–328.
16 D. Michel, M. Perezyjorba and R. Collongues, *J. Raman Spectrosc.*, 1976, **5**, 163–180.
17 J. Gu, L. Jiang, S. A. Ismail, H. Guo and D. Han, *Adv. Mater. Interfaces*, 2022, **10**, 2201764.
18 S. P. S. Badwal, *Solid State Ionics*, 1992, **52**, 23–32.
19 N. Q. Minh, *J. Am. Ceram. Soc.*, 1993, **76**, 563–588.
20 R. Khanna, T. R. Welberry and R. L. Withers, *J. Phys.: Condens. Matter*, 1993, **5**, 4251–4262.
21 M. O. Zacate, L. Minervini, D. J. Bradfield, R. W. Grimes and K. E. Sickafus, *Solid State Ionics*, 2000, **128**, 243–254.
22 T. H. Etsell and S. N. Flengas, *Chem. Rev.*, 1970, **70**, 339–376.
23 P. Li, I. W. Chen and J. E. Penner-Hahn, *Phys. Rev. B: Condens. Matter Mater. Phys.*, 1993, **48**, 10074–10081.
24 E. A. Agarkova, M. A. Borik, T. V. Volkova, A. V. Kulebyakin, I. E. Kuritsyna, E. E. Lomonova, F. O. Milovich, V. A. Myzina, P. A. Ryabochkina and N. Y. Tabachkova, *J. Solid State Electrochem.*, 2019, **23**, 2619–2626.
25 M. Hartmanova, F. Kubel, V. Burskova, M. Jergel, V. Navratil, E. E. Lomonova, K. Navratil, F. Kundracik and I. Kosti, *Russ. J. Electrochem.*, 2007, **43**, 381–389.
26 S. Kim, H. J. Avila-Paredes, S. Z. Wang, C. T. Chen, R. A. De Souza, M. Martin and Z. A. Munir, *Phys. Chem. Chem. Phys.*, 2009, **11**, 3035–3038.
27 B. C. H. Steele, *Solid State Ionics*, 2000, **134**, 3–20.
28 J. B. Goodenough, *Annu. Rev. Mater. Res.*, 2003, **33**, 91–128.
29 S. Stotz and C. Wagner, *Ber. Bunsen. Phys. Chem.*, 1966, **70**, 781–788.
30 C. Wagner, *Ber. Bunsen. Phys. Chem.*, 1968, **72**, 778–781.
31 T. Yamaguchi, T. Ishiyama, H. Kishimoto, K. Develos-Bagarinao and K. Yamaji, *Solid State Ionics*, 2020, **354**, 115414.
32 T. Ishigaki, S. Yamauchi, K. Kishio, K. Fueki and H. Iwahara, *Solid State Ionics*, 1986, **21**, 239–241.
33 Y. Aboura and K. L. Moore, *Appl. Surf. Sci.*, 2021, **557**, 149736.
34 T. Yamaguchi, T. Ishiyama, H. Kishimoto, K. Develos-Bagarinao and K. Yamaji, *Solid State Ionics*, 2022, **374**, 115819.
35 N. Sakai, K. Yamaji, T. Horita, H. Kishimoto, Y. P. Xiong and H. Yokokawa, *Solid State Ionics*, 2004, **175**, 387–391.
36 L. Bay, T. Horita, N. Sakai, M. Ishikawa, K. Yamaji and H. Yokokawa, *Solid State Ionics*, 1998, **113**, 363–367.
37 A. G. Marinopoulos, *Solid State Ionics*, 2018, **315**, 116–125.
38 W. Munch, K. D. Kreuer, G. Seifertli and J. Majer, *Solid State Ionics*, 1999, **125**, 39–45.
39 W. Munch, K. D. Kreuer, G. Seifert and J. Maier, *Solid State Ionics*, 2000, **136**, 183–189.
40 J. A. Dawson and I. Tanaka, *J. Mater. Chem. A*, 2014, **2**, 1400–1408.
41 J. A. Dawson, H. Chen and I. Tanaka, *Phys. Chem. Chem. Phys.*, 2014, **16**, 4814–4822.
42 R. Merkle, M. F. Hoedl, G. Raimondi, R. Zohourian and J. Maier, *Annu. Rev. Mater. Res.*, 2021, **51**, 461–493.
43 M. Miyamoto, A. Hamajima, Y. Oumi and S. Uemiya, *Int. J. Hydrogen Energy*, 2018, **43**, 730–738.
44 T. S. Bjørheim, M. F. Hoedl, R. Merkle, E. A. Kotomin and J. Maier, *J. Phys. Chem. C*, 2019, **124**, 1277–1284.
45 Y. Hinuma, T. Toyao, T. Kamachi, Z. Maeno, S. Takakusagi, S. Furukawa, I. Takigawa and K. Shimizu, *J. Phys. Chem. C*, 2018, **122**, 29435–29444.
46 Y. Nigara, *Solid State Ionics*, 2004, **171**, 61–67.
47 L. Gerward, J. Staun Olsen, L. Petit, G. Vaitheeswaran, V. Kanchana and A. Svane, *J. Alloys Compd.*, 2005, **400**, 56–61.
48 G. A. Kourouklis, A. Jayaraman and G. P. Espinosa, *Phys. Rev. B: Condens. Matter Mater. Phys.*, 1988, **37**, 4250–4253.
49 K. Wincewicz and J. Cooper, *J. Power Sources*, 2005, **140**, 280–296.
50 J. W. Fergus, *J. Power Sources*, 2006, **162**, 30–40.
51 S. Ramesh, V. P. Kumar, P. Kistaiah and C. V. Reddy, *Solid State Ionics*, 2010, **181**, 86–91.
52 Y. Zheng, M. Zhou, L. Ge, S. Li, H. Chen and L. Guo, *J. Alloys Compd.*, 2011, **509**, 546–550.
53 N. K. Singh, P. Singh, M. K. Singh, D. Kumar and O. Parkash, *Solid State Ionics*, 2011, **192**, 431–434.
54 N. Singh, O. Parkash and D. Kumar, *Ionics*, 2012, **19**, 165–170.
55 R. Doshi, V. L. Richards, J. D. Carter, X. P. Wang and M. Krumpelt, *J. Electrochem. Soc.*, 1999, **146**, 1273–1278.
56 N. Ai, Z. Lü, K. Chen, X. Huang, B. Wei, Y. Zhang, S. Li, X. Xin, X. Sha and W. Su, *J. Power Sources*, 2006, **159**, 637–640.
57 M. Coduri, P. Masala, M. Allieta, I. Peral, M. Brunelli, C. A. Biffi and M. Scavini, *Inorg. Chem.*, 2018, **57**, 879–891.
58 M. Coduri, M. Scavini, M. Allieta, M. Brunelli and C. Ferrero, *Chem. Mater.*, 2013, **25**, 4278–4289.
59 A. Kossoy, Q. Wang, R. Korobko, V. Grover, Y. Feldman, E. Wachtel, A. K. Tyagi, A. I. Frenkel and I. Lubomirsky, *Phys. Rev. B: Condens. Matter Mater. Phys.*, 2013, **87**, 054101.
60 A. Banerji, V. Grover, V. Sathe, S. K. Deb and A. K. Tyagi, *Solid State Commun.*, 2009, **149**, 1689–1692.
61 E. R. Andrievskaya, O. A. Kornienko, O. I. Bykov, A. V. Sameliuk and Z. D. Bohatyriova, *J. Eur. Ceram. Soc.*, 2019, **39**, 2930–2935.
62 N. Sakai, K. Yamaji, T. Horita, H. Yokokawa, Y. Hirata, S. Sameshima, Y. Nigara and J. Mizusaki, *Solid State Ionics*, 1999, **125**, 325–331.
63 H. Yokokawa, T. Horita, N. Sakai, K. Yamaji, M. Brito, Y. Xiong and H. Kishimoto, *Solid State Ionics*, 2004, **174**, 205–221.
64 Y. P. Xiong, K. Yamaji, T. Horita, N. Sakai and H. Yokokawa, *J. Electrochem. Soc.*, 2002, **149**, E450–E454.
65 Y. Nigara, K. Kawamura, T. Kawada, J. Mizusaki and M. Ishigame, *J. Electrochem. Soc.*, 1999, **146**, 2948–2953.

© 2024 The Author(s). Published by the Royal Society of Chemistry

Open Access Article. Published on 08 September 2023. Downloaded on 6/11/2026 10:35:40 PM. This article is licensed under a Creative Commons Attribution 3.0 Unported Licence.

66 Y. Nigara, *Solid State Ionics*, 2003, **159**, 135–141.
67 Y. Nigara, K. Kawamura, T. Kawada and J. Mizusaki, *Solid State Ionics*, 2000, **136**, 215–221.
68 Y. Nigara, K. Yashiro, T. Kawada and J. Mizusaki, *Solid State Ionics*, 2001, **145**, 365–370.
69 V. Besikiotis, C. S. Knee, I. Ahmed, R. Haugsrud and T. Norby, *Solid State Ionics*, 2012, **228**, 1–7.
70 D. Y. Wang, D. S. Park, J. Griffith and A. S. Nowick, *Solid State Ionics*, 1981, **2**, 95–105.
71 J. Faber, C. Geoffroy, A. Roux, A. Sylvestre and P. Abelard, *Appl. Phys. A: Mater. Sci. Process.*, 1989, **49**, 225–232.
72 T. Norby, M. Wideroe, R. Glockner and Y. Larring, *Dalton Trans.*, 2004, 3012–3018.
73 L. E. Kalland, A. Loken, T. S. Bjorheim, R. Haugsrud and T. Norby, *Solid State Ionics*, 2020, **354**, 115401.
74 S. A. Ismail, L. L. Jiang, P. Zhong, T. Norby and D. L. Han, *J. Alloys Compd.*, 2022, **899**, 163306.
75 S. A. Ismail and D. L. Han, *J. Am. Ceram. Soc.*, 2022, **105**, 7548–7557.
76 W. Sun, S. Fang, L. Yan and W. Liu, *Fuel Cells*, 2012, **12**, 457–463.
77 T. Shimura, M. Komori and H. Iwahara, *Solid State Ionics*, 1996, **86–88**, 685–689.
78 T. Omata, *Solid State Ionics*, 2004, **167**, 389–397.
79 G. B. D. Huo, D. Siméone, H. Khodja and S. Surblé, *ECS Meeting Abstracts*, 2015, **MA2015-03**, 405.
80 E. Antonova, E. Tropin and A. Khodimchuk, *Ionics*, 2022, **28**, 5181–5188.
81 T. Omata and S. Otsuka-Yao-Matsuo, *J. Electrochem. Soc.*, 2001, **148**, E252–E261.
82 Q. A. Islam, S. Nag and R. N. Basu, *Mater. Res. Bull.*, 2013, **48**, 3103–3107.
83 E. P. Antonova, M. V. Ananyev, A. S. Farlenkov, E. S. Tropin, A. V. Khodimchuk and N. M. Porotnikova, *Russ. J. Electrochem.*, 2017, **53**, 651–657.
84 D. Han, K. Kojima, M. Majima and T. Uda, *J. Electrochem. Soc.*, 2014, **161**, F977–F982.
85 T. Omata, K. Okuda, S. Tsugimoto and S. Otsuka-Matsuo-Yao, *Solid State Ionics*, 1997, **104**, 249–258.
86 E. P. Antonova, A. S. Farlenkov, E. S. Tropin, V. A. Eremin, A. V. Khodimchuk and M. V. Ananyev, *Solid State Ionics*, 2017, **306**, 112–117.
87 M. Pirzada, R. W. Grimes, L. Minervini, J. F. Maguire and K. E. Sickafus, *Solid State Ionics*, 2001, **140**, 201–208.
88 M. E. Björketun, C. S. Knee, B. J. Nyman and G. Wahnström, *Solid State Ionics*, 2008, **178**, 1642–1647.
89 B. J. Nyman, M. E. Björketun and G. Wahnström, *Solid State Ionics*, 2011, **189**, 19–28.
90 K. Toyoura, A. Nakamura and K. Matsunaga, *J. Phys. Chem. C*, 2015, **119**, 8480–8487.
91 M. P. Vandijk, K. J. Devries and A. J. Burggraaf, *Solid State Ionics*, 1983, **9–10**, 913–919.
92 V. A. Vorotnikov, S. A. Belyakov, M. S. Plekhanov, A. Y. Stroeva, A. S. Lesnichyova, O. M. Zhigalina, D. N. Khmelenin, A. V. Atanova, V. G. Basu and A. V. Kuzmin, *Ceram. Int.*, 2022, **48**, 35166–35175.
93 J. A. Labrincha, J. R. Frade and F. M. B. Marques, *Solid State Ionics*, 1997, **99**, 33–40.
94 D. L. Han, K. Kato and T. Uda, *Chem. Commun.*, 2017, **53**, 12684–12687.
95 X. R. Zhang, L. L. Jiang, S. H. Guo and D. L. Han, *ChemSusChem*, 2022, **15**, e202201879.
96 D. L. Han, P. Zhong, X. R. Zhang and L. L. Jiang, *J. Mater. Chem. A*, 2022, **10**, 8887–8897.
97 Y. Okuyama, T. Kozai, S. Ikeda, M. Matsuka, T. Sakai and H. Matsumoto, *Electrochim. Acta*, 2014, **125**, 443–449.
98 A. Magraso, *J. Power Sources*, 2013, **240**, 583–588.
99 R. Haugsrud and T. Norby, *Nat. Mater.*, 2006, **5**, 193–196.
100 A. V. Shlyakhtina, J. C. C. Abrantes, E. Gomes, N. V. Lyskov, E. Y. Konysheva, S. A. Chernyak, E. P. Kharitonova, O. K. Karyagina, I. V. Kolbanev and L. G. Shcherbakova, *Materials*, 2019, **12**, 2452.
101 A. V. Shlyakhtina, N. V. Lyskov, E. Y. Konysheva, S. A. Chernyak, I. V. Kolbanev, G. A. Vorobieva and L. G. Shcherbakova, *J. Solid State Electrochem.*, 2020, **24**, 1475–1486.
102 K. E. J. Eurenius, E. Ahlberg and C. S. Knee, *Solid State Ionics*, 2010, **181**, 1258–1263.
103 K. E. J. Eurenius, E. Ahlberg and C. S. Knee, *Solid State Ionics*, 2010, **181**, 1577–1585.
104 H. Fjeld, R. Haugsrud, A. Gunnas and T. Norby, *Solid State Ionics*, 2008, **179**, 1849–1853.
105 K. E. J. Eurenius, E. Ahlberg, I. Ahmed, S. G. Eriksson and C. S. Knee, *Solid State Ionics*, 2010, **181**, 148–153.
106 K. E. J. Eurenius, H. K. Bentzer, N. Bonanos, E. Ahlberg and C. S. Knee, *J. Solid State Electrochem.*, 2010, **15**, 2571–2579.
107 K. E. J. Eurenius, E. Ahlberg and C. S. Knee, *Dalton Trans.*, 2011, **40**, 3946–3954.
108 T. S. Bjorheim, V. Besikiotis and R. Haugsrud, *Dalton Trans.*, 2012, **41**, 13343–13351.
109 Y. Ling, J. Chen, Z. Wang, C. Xia, R. Peng and Y. Lu, *Int. J. Hydrogen Energy*, 2013, **38**, 7430–7437.
110 Y. Wu, Z. Gong, J. Hou, L. Miao, H. Tang and W. Liu, *Int. J. Hydrogen Energy*, 2019, **44**, 13835–13842.
111 T. Tu, J. Liu and K. Peng, *Ceram. Int.*, 2017, **43**, 16384–16390.
112 B. Zhang, K. Wu and K. Peng, *J. Power Sources*, 2018, **399**, 157–165.
113 Z. Zhong, Y. Jiang, Z. Lian, X. Song and K. Peng, *Ceram. Int.*, 2020, **46**, 12675–12685.
114 Z. Tao, L. Bi, S. Fang and W. Liu, *J. Power Sources*, 2011, **196**, 5840–5843.
115 T. Tu, B. Zhang, J. Liu, K. Wu and K. Peng, *Electrochim. Acta*, 2018, **283**, 1366–1374.
116 B. Zhang, Z. Zhong, T. Tu, K. Wu and K. Peng, *J. Power Sources*, 2019, **412**, 631–639.
117 M. Zhang, D. Wang, L. Miao, Z. Jin, K. Dong and W. Liu, *Electrochem. Commun.*, 2021, **126**, 107026.
118 Z. Tao, L. Yan, J. Qiao, B. Wang, L. Zhang and J. Zhang, *Prog. Mater. Sci.*, 2015, **74**, 1–50.
119 H. Matsumoto, S. Okada, S. Hashimoto, K. Sasaki, R. Yamamoto, M. Enoki and T. Ishihara, *Ionics*, 2007, **13**, 93–99.

© 2024 The Author(s). Published by the Royal Society of Chemistry

Open Access Article. Published on 08 September 2023. Downloaded on 6/11/2026 10:35:40 PM.
This article is licensed under a Creative Commons Attribution 3.0 Unported Licence.

120 S. Fang, L. Bi, C. Yang, L. Yan, C. Chen and W. Liu, *J. Alloys Compd.*, 2009, **475**, 935–939.
121 L. Yan, W. Sun, L. Bi, S. Fang, Z. Tao and W. Liu, *Int. J. Hydrogen Energy*, 2010, **35**, 4508–4511.
122 J. W. Phair and S. P. S. Badwal, *Ionics*, 2006, **12**, 103–115.
123 S. Fang, L. Bi, L. Yan, W. Sun, C. Chen and W. Liu, *J. Phys. Chem. C*, 2010, **114**, 10986–10991.
124 Z. Zhu, W. Sun, Z. Wang, J. Cao, Y. Dong and W. Liu, *J. Power Sources*, 2015, **281**, 417–424.
125 Z. Zhu, L. Yan, H. Liu, W. Sun, Q. Zhang and W. Liu, *Int. J. Hydrogen Energy*, 2012, **37**, 12708–12713.
126 W. Sun, Z. Shi and W. Liu, *J. Electrochem. Soc.*, 2013, **160**, F585–F590.
127 Y. Nigara, J. Mizusaki, K. Kawamura, T. Kawada and M. Ishigame, *Solid State Ionics*, 1998, **113**, 347–354.
128 F. Liu, D. Ding and C. Duan, *Adv. Sci.*, 2023, **10**, e2206478.
129 I. A. Amar, R. Lan, C. T. G. Petit and S. Tao, *J. Solid State Electrochem.*, 2011, **15**, 1845–1860.
130 G. Marnellos, S. Zisekas and M. Stoukides, *J. Catal.*, 2000, **193**, 80–87.
131 G. Marnellos and M. Stoukides, *Science*, 1998, **282**, 98–100.
132 L. Zhu, C. Cadigan, C. Duan, J. Huang, L. Bian, L. Le, C. H. Hernandez, V. Avance, R. O'Hayre and N. P. Sullivan, *Commun. Chem.*, 2021, **4**, 121.
133 C. Chen and G. L. Ma, *J. Alloys Compd.*, 2009, **485**, 69–72.
134 W. B. Wang, X. B. Cao, W. J. Gao, F. Zhang, H. T. Wang and G. L. Ma, *J. Membr. Sci.*, 2010, **360**, 397–403.
135 T. N. Ye, S. W. Park, Y. F. Lu, J. Li, M. Sasase, M. Kitano and H. Hosono, *J. Am. Chem. Soc.*, 2020, **142**, 14374–14383.
136 J. Will, A. Mitterdorfer, C. Kleinlogel, D. Perednis and L. J. Gauckler, *Solid State Ionics*, 2000, **131**, 79–96.
137 P. Kuntke, M. R. Arredondo, L. Widyakristi, A. ter Heijne, T. H. J. A. Sleutels, H. V. M. Hamelers and C. J. N. Buisman, *Environ. Sci. Technol.*, 2017, **51**, 3110–3116.
138 Y. Xie, *Solid State Ionics*, 2004, **168**, 117–121.
139 J.-D. Wang, Y.-H. Xie, Z.-F. Zhang, R.-Q. Liu and Z.-J. Li, *Mater. Res. Bull.*, 2005, **40**, 1294–1302.
140 R. Liu, Y. Xie, J. Wang, Z. Li and B. Wang, *Solid State Ionics*, 2006, **177**, 73–76.
141 D. L. Han and T. Uda, *J. Mater. Chem. A*, 2018, **6**, 18571–18582.